TECHNISCHE UNIVERSITÄT WIEN
Vienna University of Technology

DIPLOMARBEIT

# Transport current anisotropy in melt-textured high-temperature superconductors

Ausgeführt am Atominstitut der Österreichischen Universitäten

unter der Anleitung von

Privatdoz. Dipl.-Ing. Dr.techn. Michael Eisterer

durch

Thomas Baumgartner

Düsseldorfstraße 5-13/2/22
1220 Wien, Österreich

Wien, am 1. Dezember 2009.

# Acknowledgments

I would like to thank my diploma thesis advisor Michael Eisterer for always taking the time to give advice and render assistance, and for making this experience pleasant by being the easy-going and humorous person that he is.

My gratitude also goes to Florian Hengstberger for his gnuplot and LaTeX tips, Tom Withnell for showing me how to perform measurements with the superconducting magnet system and for proofreading my diploma thesis, Johann Emhofer for his help with Solid Edge, and all the other colleagues at the low temperature lab, who have been very kind and supportive.

Furthermore, I would like to express my appreciation for my girlfriend Doris and all my other friends, who have enriched my life in many ways.

With special gratitude I wish to thank my parents for making my educational path possible and for their constant, unconditional support throughout all these years.

## Abstract

The main objective of the diploma thesis at hand was to measure the dependence of the critical current in melt-textured high-temperature superconductors on the angle between an external magnetic field and the crystallographic *ab*-plane of the superconductor, which is called transport current anisotropy. To that end, a suitable sample preparation method which includes sputter deposition of silver contacts had to be devised. Contact resistances of the order of $10^{-9}$ $\Omega\mathrm{m}^2$ between these silver contacts and the superconductor were achieved by this method. The transport current anisotropy of melt-textured YBCO was measured at a temperature of 77 K and magnetic fields of up to 6 T. Anomalous transitions from the superconducting to the dissipative state were observed in some of the measurements and resulted in an unexpected shape of the corresponding anisotropy curves. These transitions were ascribed to the effect of Joule heating in the contact areas, as supported by the experimental data.

# Contents

# 1. Timetable and material costs estimate

Prior to beginning with sample preparation and experiments, a timetable consisting of several project milestones and their scheduled completion dates as well as a material cost estimate were worked out. Table 1.1 compares the initial schedule to the actual completion dates. Note that some of the milestones and their scheduled completion dates had to be changed during the course of the experiments, since the strategy for achieving the desired results was not known in detail when the first version of the timetable was compiled. In total I spent approximately 480 hours on preparing samples, planning experiments and performing the actual measurements.

A cost estimate of the materials which were required for sample preparation and experiments is given in table 1.2. Materials such as indium wire, Kapton tape, silver conductive paint, abrasive paper, acetone, and paper wipes, which were used in small quantities, are summarized under the item "Consumables". Note that the required amount of liquid nitrogen is an estimate, since the available nitrogen Dewars were not equipped with level meters.

| Milestone | Scheduled date | Actual date |
|---|---|---|
| Rough outline of the experimental tasks | 11.03.2009 | 12.03.2009 |
| Competency to operate the sputtering machine of the institute | 13.03.2009 | 11.03.2009 |
| Competency to cut, grind, and glue YBCO | 20.03.2009 | 19.03.2009 |
| Determination of the silver deposition rate of the sputtering machine | 25.03.2009 | 24.03.2009 |
| First sputtering test with an YBCO sample | 26.03.2009 | 26.03.2009 |
| Completion of the sample tray | 30.03.2009 | 23.03.2009 |
| Completion of the contact assembly | 03.04.2009 | 03.04.2009 |
| Determination of the indium-YBCO contact resistance | 22.04.2009 | 23.04.2009 |
| Determination of the pressure dependence of the copper-indium contact resistance | 27.04.2009 | 23.04.2009 |
| Determination of the influence of glow discharge cleaning | 30.04.2009 | 04.05.2009 |
| Determination of sputtering parameters suitable for sample preparation | 08.05.2009 | 01.07.2009* |
| First high current test in liquid nitrogen | 25.05.2009 | 26.05.2009 |
| Determination of the indium-silver and silver-YBCO contact resistance | 05.06.2009 | 16.06.2009** |
| Suitable sample preparation process with reproducible results | 26.06.2009 | 01.07.2009 |
| Completion of the anisotropy measurements | 03.08.2009 | 17.08.2009 |
| Completion of the diploma thesis | 30.09.2009 | 01.12.2009 |

* A high discharge voltage was initially used before this was identified to be unnecessary.

** The date refers to the first measurement on a sample with grooves carved into its surface.

Table 1.1.: Scheduled and actual completion dates of project milestones.

| **Item** | **Quantity** | **Costs** |
|---|---|---|
| Liquid Nitrogen | 250 l | 47.50 € |
| Liquid Helium* | 246 l | 319.80 € |
| Sputtering target, 2" diameter, 1/4" thick, 99.99% pure silver (Kurt J. Lesker Company) | 1 unit | 224.46 € |
| Materials for the construction of the sample tray and the contact assembly** | – | 25.00 € |
| Consumables (indium wire, Kapton tape, silver conductive paint, etc.)** | – | 15.00 € |
| | *Sum total:* | 631.76 € |

* With gas return, the current university internal costs were 1.30 EUR/l.

** Costs of these items were estimated.

Table 1.2.: Cost estimate of the materials that were used for sample preparation and experiments.

# 2. General information and motivation

## 2.1. Melt-textured high-temperature superconductors

All materials that are considered high-temperature superconductors[1] possess a layered crystalline structure. While single crystals can have a very high critical current density, the superconducting properties of sintered bulk materials are considerably inferior. This is caused by large grain boundary angles, which suppress the supercurrents. Since a high critical current density is crucial to many technical applications, production methods that allow the control of the grain alignment have been developed. One such method which is applicable to bulk material production (as opposed to thin films) is the top seeded melt growth (TSMG) process, which is described in the following.

TSMG utilizes the recrystallization process of a sintered pellet with the chemical composition (RE)$Ba_2Cu_3O_{7-\delta}$, where (RE) stands for a rare earth element. For this purpose, the pellet is heated above its peritectic temperature $T_p$ (960 ... 1068 °C, depending on the rare earth element), which leads to the decomposition of the pellet into a $(RE)_2BaCuO_5$ solid phase and a BaCuO-based liquid phase [1]. For the sake of shorter notations, the chemical formula of the pellet is often abbreviated to RE-123, whereas the solid phase after decomposition is named RE-211[2].

A small single crystal with lattice parameters similar to those of the target RE-123 material is placed on the top surface of the pellet prior to the melt processing, thereby providing a nucleation site. After the pellet has decomposed, its temperature is decreased below $T_p$ at a very slow rate of typically 1 °C per hour. The result is a solid RE-123 phase with inclusions of the RE-211 phase. Because of the high temperatures

[1] A critical temperature above 30 K is often used as the criterion to distinguish between high-temperature and conventional superconductivity. However, some other definitions are also common.

[2] The digits refer to the number of atoms of the rare earth element, barium, and copper within a unit cell.

involved in the production process, reoxygenation of the material is necessary in order to ensure good superconducting properties. Unlike in the original pellet, the grains of the melt-textured bulk material are aligned with the seed crystal and therefore with one another. However, the homogeneity of the material is disturbed by inclusions of the RE-211 phase. These non-superconducting inclusions cause a reduction of the superconducting volume as well as mechanical stress that can lead to cracks. Thus, it is desirable to have very small and homogeneously distributed RE-211 inclusions in the material. A material with no inclusions at all would not be desirable, since the inclusions correlate with the formation of effective flux pinning sites, thereby increasing the critical current density [1].

The parent compounds of high-temperature superconductors are Mott insulators. Such materials should exhibit metallic behavior according to their electronic band structure (half-filled band intersecting the Fermi surface), but in fact they are insulators due to the strong Coulomb repulsion of their electrons. In case of cuprate superconductors the half-filled band arises from the d-orbitals of the copper atoms, whose electron spins order antiferromagnetically. Electrical conductivity of Mott insulators can be achieved by doping, which is generally done with holes. In cuprate superconductors these holes are created in the p-orbitals of the oxygen atoms, which bind covalently to the copper d-orbitals. Doping is usually achieved by varying the oxygen content, which leads to non-stoichiometric compounds such as $YBa_2Cu_3O_{7-\delta}$ (YBCO). The Néel temperature of such compounds decreases with increasing hole concentration, until the antiferromagnetism disappears completely and the substance becomes superconducting at sufficiently low temperatures. With increasing hole concentration the critical temperature first increases, then reaches a maximum (optimal doping), and then decreases again until superconductivity is destroyed.

When a current is applied to a defect-free type II superconductor, the flux lines begin to move under the influence of the Lorentz force. This results in an electric field which accelerates the normal conducting electrons inside the superconductor, causing them to transfer energy to the lattice through inelastic collisions. If, however, the superconductor is not defect-free, the flux lines are pinned by the inhomogeneities of the material, which inhibits their movement and thereby enables lossless current transport. Since the pinning forces are finite, the flux lines can only be held in place as long as the Lorentz force does not exceed a critical value which corresponds to the so-called critical current $I_c$. If the current is increased above $I_c$, the flux lines are torn from their pinning centers, which leads to dissipation, although the material is still in its superconducting thermodynamic state. A distinctive feature of cuprate superconductors is the so-called intrinsic pinning, which occurs when an applied magnetic field is parallel to the Cu-O planes of the superconductor (which are parallel to the crystallographic $ab$-plane). In this case the layered structure of the material facilitates particularly strong pinning.

This behavior gives rise to the transport current anisotropy found in high-temperature superconductors: When the superconductor is placed in an external magnetic field which is parallel to its $ab$-plane (denoted as $H \,||\, ab$), the pinning forces inside the material are stronger than they are for other field orientations due to the layered structure of the superconductor. As a result, the critical current depends on the angle between the magnetic field and the $ab$-plane of the superconductor. Aside from the peak in critical current (density) that occurs for $H \,||\, ab$ (the so-called $ab$-peak), a peak for $H \,||\, c$ can also be observed in some cases. This $c$-axis peak is generally attributed to pinning by twin boundaries or other $c$-axis correlated defects.

Due to their relatively high critical temperatures, high-temperature superconductors can be used in a wider variety of technical applications than conventional superconductors. While the so-called coated conductors are better suited for power distribution purposes, bulk superconductors can be particularly useful for the following applications:

- Magnetic bearings (for flywheel energy storage systems, etc.)
- Motors / generators (size reduction possible due to the higher energy density of bulk superconductors)
- Trapped flux devices (superior replacements for permanent magnets in magnetic separators, magnetron sputtering systems, etc.)

## 2.2. Motivation

Knowing how the critical current (density) of a superconductor depends on the strength and direction of an applied magnetic field, is of paramount importance for technical applications. In light of the fact that a theory which explains the phenomena associated with high-temperature superconductivity in detail is yet to be developed, the experimental acquisition of such knowledge might also provide insights of theoretical value.

The transport current anisotropy of melt-textured bulk superconductors has been measured before at a temperature of 77 K and magnetic fields of up to 20 T, as reported in [2]. However, the method for contacting the samples used in these measurements was to apply silver conductive paint and anneal the samples at 900 °C. This method necessitates reoxygenation due to the oxygen depletion caused by the high annealing temperature, resulting in a rather lengthy (reoxygenation may take several days) sample preparation process.

The motivation for the diploma thesis at hand was to demonstrate the feasibility of sputter deposition as a means for contacting samples, and to gather more experimental data on the behavior of melt-textured high-temperature superconductors. Since bulk superconductors are usually characterized magnetically (which does not allow to derive their anisotropy), performing transport current anisotropy measurements is an important step towards a comprehensive understanding of the behavior of such materials.

## 2.3. The bulk used for sample preparation

The investigated samples were cut from a cylindrical bulk, which will be referred to as "bulk cylinder" henceforth. This bulk cylinder was manufactured using the TSMG method described in section 2.1. Its diameter was one inch (25.4 mm) and its symmetry axis was perpendicular to the $ab$-plane. The raw material was $YBa_2Cu_3O_{7-\delta}$ (YBCO), which means that the rare earth element previously denoted by (RE) was yttrium in this case, and the final product was a melt-textured Y-123 bulk with Y-211 inclusions. YBCO crystallizes in a layered defect perovskite structure. It is a type II superconductor and the first material which was discovered to become superconducting above 77 K[3].

YBCO is a non-stoichiometric compound, which means that due to its oxygen deficiency $\delta$ the number of oxygen atoms in the formula $YBa_2Cu_3O_{7-\delta}$ is not an integer value. For the material to be superconducting, the condition $\delta \leq 0.65$ must be met, since this will enforce an orthorhombic crystal structure, whereas a higher oxygen deficiency causes the material to crystallize in the non-superconducting tetragonal phase (see figure 2.2). Optimal superconducting properties are exhibited for $\delta = 0.07$. Unfortunately, the oxygen deficiency of the bulk cylinder that was used for sample preparation was unknown. Data on the size and density of Y-211 inclusions were also not available. Some important properties of YBCO (assuming optimal oxygen doping) are shown in table 2.1 (taken from [3]). Note that the anisotropy $\gamma$ in table 2.1 is defined by the coherence lengths and is not the same value as the critical current anisotropy $\gamma_{cc}$ (see section 4.4). With respect to sample storage, it is also relevant to know that YBCO is sensitive to degradation from humidity [4].

[3] This temperature is important from a technological point of view, since it is the boiling point of liquid nitrogen at atmospheric pressure.

| **Material property** | **Symbol** | **Typical value** |
|---|---|---|
| Critical temperature | $T_c$ | 92 K |
| Lower critical field parallel to the $c$-axis | $B_{c1}$ $(H \,\|\|\, c)$ | 38 mT |
| Lower critical field parallel to the $ab$-plane | $B_{c1}$ $(H \,\|\|\, ab)$ | 7.4 mT |
| Upper critical field parallel to the $c$-axis | $B_{c2}$ $(H \,\|\|\, c)$ | 150 T |
| Upper critical field parallel to the $ab$-plane | $B_{c2}$ $(H \,\|\|\, ab)$ | 1100 T |
| Coherence length parallel to the $c$-axis | $\xi_c$ | 0.2 nm |
| Coherence length parallel to the $ab$-plane | $\xi_{ab}$ | 1.5 nm |
| Penetration depth parallel to the $c$-axis | $\lambda_c$ | 1040 nm |
| Penetration depth parallel to the $ab$-plane | $\lambda_{ab}$ | 140 nm |
| Anisotropy | $\gamma$ | 7.4 |

Table 2.1.: Properties of optimally doped YBCO single crystals.

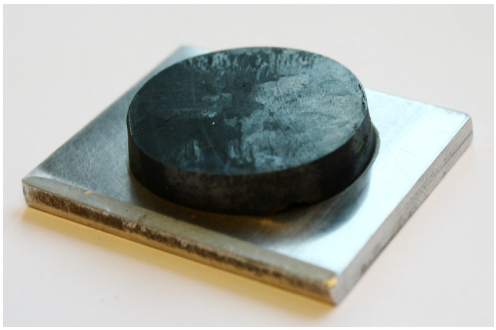

Figure 2.1.: YBCO bulk cylinder mounted on an aluminum plate.

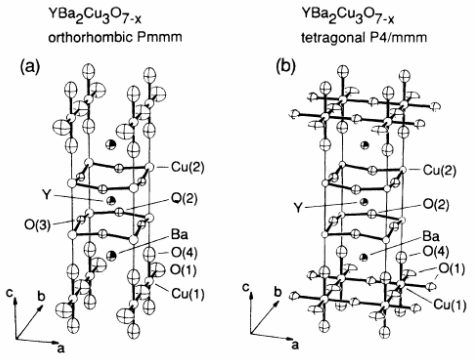


Figure 2.2.: Crystal structure of the two possible phases of YBCO.

# 3. Sample preparation and measurements

## 3.1. Mechanical sample preparation

The steps required to produce samples which are ready for the sputter deposition of silver contacts (see section 3.4) are described in the following.

### 3.1.1. Cutting and gluing samples

Since the geometry of the bulk cylinder (see section 2.3) was not suitable for the intended measurements, bar-shaped samples were cut out of the cylinder. For this purpose, a threaded aluminum block was heated to approximately 100 °C on a hot plate. A small amount of LOC wax was then placed on the block. When the wax was molten, the YBCO cylinder was placed on the aluminum block and both were removed from the hot plate. After the aluminum block and the cylinder had cooled down to room temperature, the wax glued them together firmly.

An Isomet low speed saw with a diamond saw blade was used to cut the bulk cylinder into discs as shown in figure 3.2. The thread in the aluminum block was used to attach the block to the saw. The saw was operated at a speed setting of 4 out of 10, which corresponds to roughly 200 rpm. At this speed, cutting an YBCO cylinder with a diameter of one inch may take up to three hours if no additional weight is used to press the cylinder against the saw blade. A disc thickness of 0.2 mm was achieved without damaging the disc during the cutting process. However, it may not be desirable to produce such thin samples for reasons of mechanical stability (see samples 0625A and 0625B in section 3.8).

After cutting a disc from the cylinder, the oil which lubricates the saw blade must be removed from the superconductor. Isopropyl alcohol is suitable for this task. The YBCO disc can then be mounted on an aluminum block using LOC wax in the same way as described above. This aluminum block was attached to the saw again and

two 5 mm wide bars were cut out of each disc (see figure 3.1). These YBCO bars were then removed from the aluminum block by heating it with a hot plate. While the LOC wax is still liquid, it can be removed from the bars with a cotton swab.

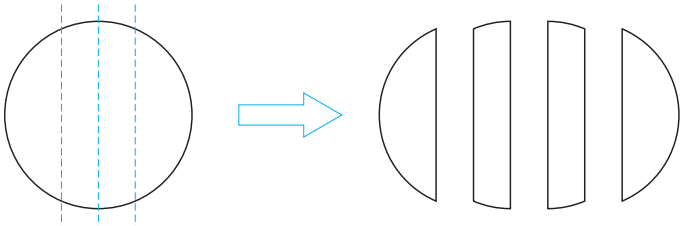

Figure 3.1.: Cutting of YBCO discs. The two middle bars undergo further processing and are used for measurements.

The cleaned bars were glued onto 1 mm thick glass-reinforced epoxy base plates (see figure 3.3) which facilitated the handling and provided sufficient mechanical stability. This material was chosen because its relative thermal expansion $\frac{\Delta L}{L}$ that occurs when cooling it from room temperature to 77 K is approximately $-2.0 \cdot 10^{-3}$ [5], which is similar to that of YBCO [6]. Low temperature varnish C5-101 from Oxford Instruments was used as an adhesive. The drying time was shortened to roughly 10 min by placing the epoxy plates on a hot plate which was set to approximately 80 °C. Each YBCO bar and its epoxy base plate will be referred to as a sample with a unique name (which is derived from its production date) in the following sections.

### 3.1.2. Grinding and carving grooves into samples

A flat sample surface is desirable in case pressure contacts are used, as it was done in the contact resistance and anisotropy measurements (see sections 3.5 and 3.7). It is therefore prudent to grind a sample with abrasive paper in case its surface is uneven due to imperfections of the cutting process. Using grinding to significantly reduce the thickness of an YBCO bar is not practical, as the process is very time consuming due to the high grit number required (#500 or higher). Using abrasive paper with a lower grit number tends to tear grains of YBCO out of the surface, leaving little "craters" behind.

Using a very high grit number (e.g. #2400) was found to have a negative effect on the adhesion of the sputter deposited silver contacts and their contact resistance.

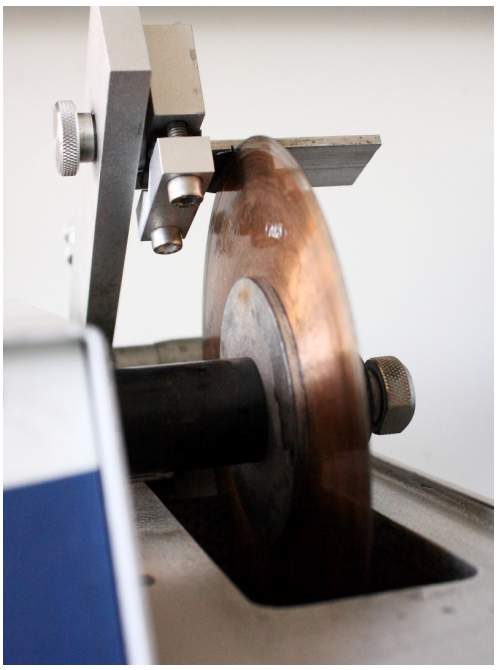

Figure 3.2.: Low speed saw used for cutting discs from the bulk cylinder.

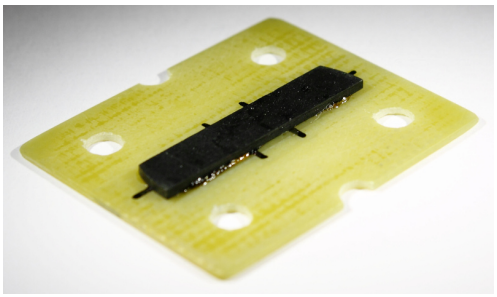

Figure 3.3.: Sample 0402A, consisting of an YBCO bar and an epoxy base plate.

This is consistent with an observation in [7], stating that roughening of the substrate surface tends to promote better adhesion of the sputter deposited layer. In order to roughen the surface without producing the aforementioned craters, grooves were carved into the surfaces of the samples. These grooves also serve to enlarge the effective contact area of the silver layer and the superconductor, thereby lowering the contact resistance. The grooves were carved with a diamond tip pen, which was scratched across the surface along a plastic ruler. Approximately four grooves per millimeter were carved in the direction of the current as well as perpendicular to it, producing a square pattern on the surface of the sample as shown in figures 3.4 and 3.6. The grooves were approximately 20 µm wide and 10 µm deep.

### 3.1.3. Milling bridges into samples

High critical current densities were expected under the conditions of the planned anisotropy measurements. Since the power dissipation (and therefore the Joule heating) in the current contacts scales with the square of the transport current, it seemed reasonable to decrease the critical current by reducing the cross section of the superconductor.

Since the YBCO bars could not be cut arbitrarily thin, the only remaining option was to reduce their width. Doing so with the entire bar would result in a smaller contact area and therefore a higher contact resistance. Therefore, bridges were milled into the samples, leaving the contact areas unchanged while reducing the cross section of the superconductor between the voltage contacts. A width of 2 mm was chosen for the bridges, which corresponds to a cross section reduction factor of 2.5, given the initial bar width of 5 mm. The shape of a sample with a bridge is shown in figure 3.5, and a microscope photograph of such a bridge is depicted in figure 3.7. Note that the milling was done after sputtering and measuring the contact resistance to make sure the sample is worth the additional time investment.

Figure 3.4.: Schematic view of the grooves (distance exaggerated for clarity) which were carved into the samples with a diamond tip pen.

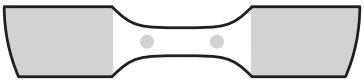

Figure 3.5.: The cross section of a sample can be reduced by milling a bridge into the YBCO. The sputter deposited current and voltage contacts are indicated by gray areas.

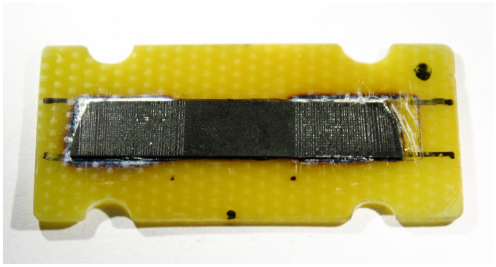

Figure 3.6.: Sample 0703A after grooves were carved into its surface.

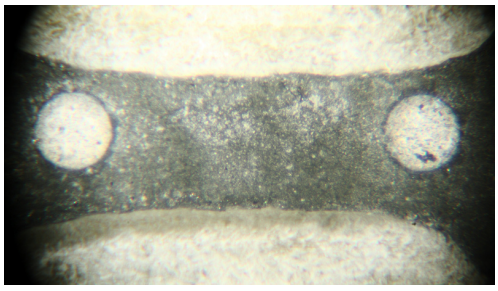

Figure 3.7.: Microscope picture of the bridge of sample 0625B. The two circles are the sputtered voltage contacts.

## 3.2. Construction of the contact assembly

In order to perform contact resistance measurements (see sections 3.5 and 4.2), a reproducible method for contacting the samples was required. For this purpose, a contact assembly was constructed, which consists of two parts: the contact plate and the stabilizer plate. The contact plate is a rectangular piece of 3 mm thick glass-reinforced epoxy board, manufactured by Isovolta under the brand name Isoval 10. Four tiles were cut out of a 0.5 mm thick copper sheet and were then glued onto the Isoval 10 plate with low temperature varnish. Two of them serve as current leads, whereas the other two can be used to establish electrical contact with the voltage contacts of a sample. Six holes were drilled into the contact plate, four of which are for the screws that press a sample against the copper contacts, whereas the other two allow contacting a sample directly by means of a wire.

The stabilizer plate is a 4 mm thick rectangular piece of aluminum. Four M3 threads were cut into it, which allow the contact plate to be screwed down to the stabilizer plate, thus pressing a sample between the two plates against the current leads. Indium pads were used as mechanical buffers between the samples and the current leads, as described in section 3.5. Two 3D views of the Solid Edge[1] model of the contact assembly are shown in figures 3.8 and 3.9. A 2D draft of the parts the contact assembly consists of, which includes their physical dimensions, is depicted on page 19. Photographs of the contact assembly can be found in section 3.5.

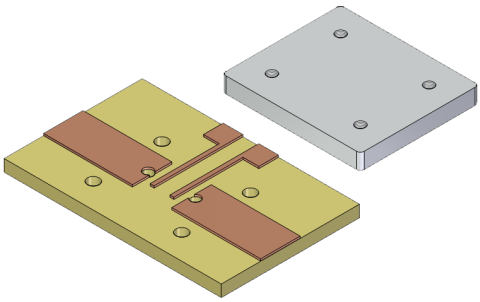

Figure 3.8.: The components of the contact assembly: contact plate and stabilizer plate. The two wider copper tiles are the current leads.

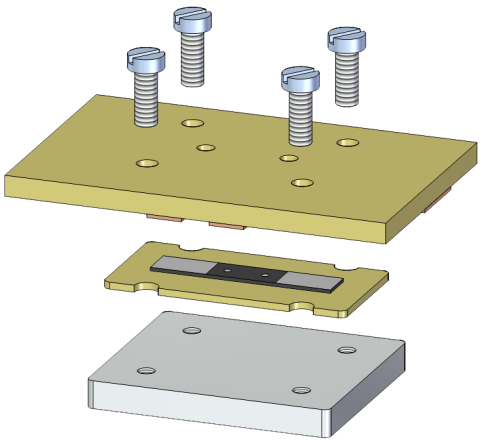

Figure 3.9.: Exploded view of the contact assembly and a sample.

[1] CAD software used in the design of the contact assembly and the sample tray.

| REVISION HISTORY | | | |
|---|---|---|---|
| REV | DESCRIPTION | DATE | APPROVED |
| | | | |

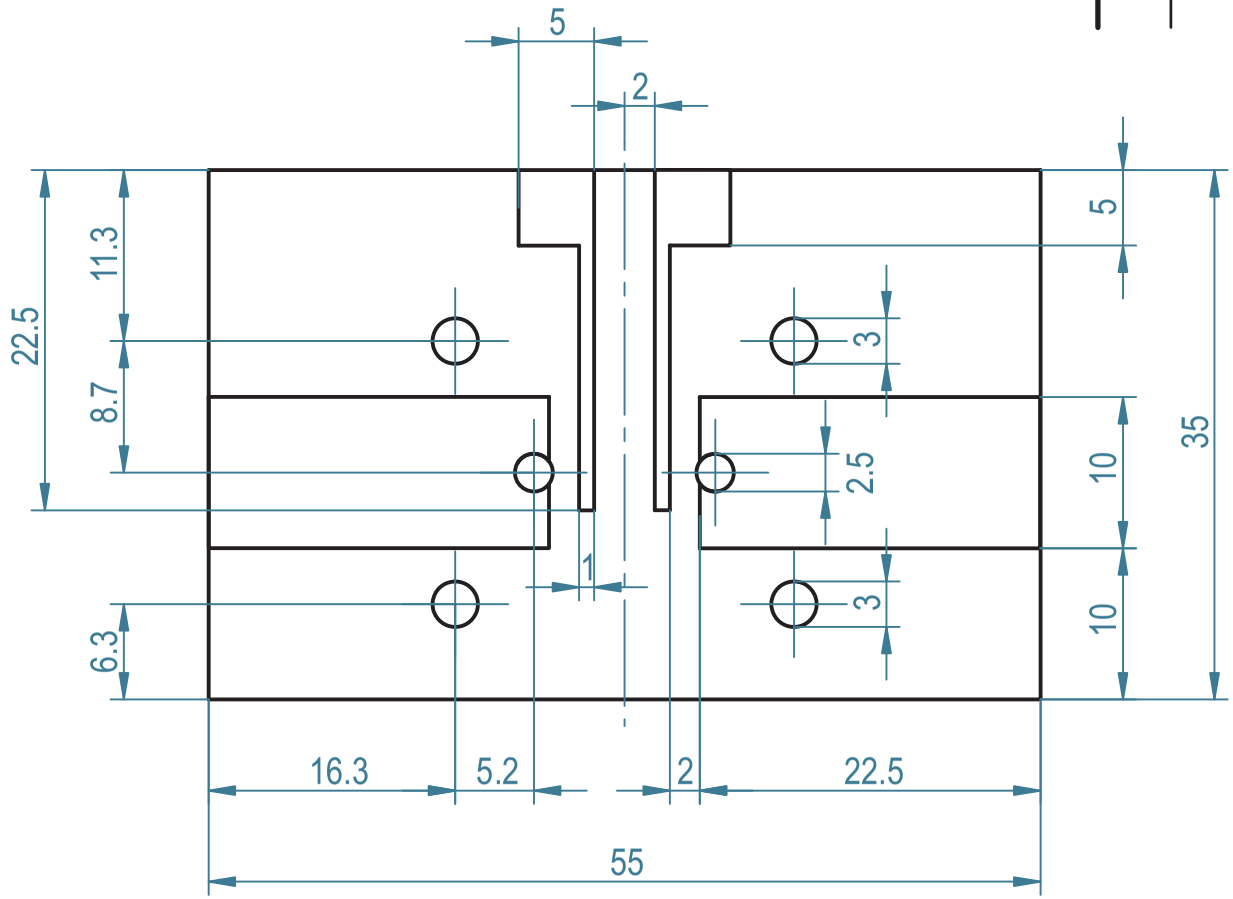


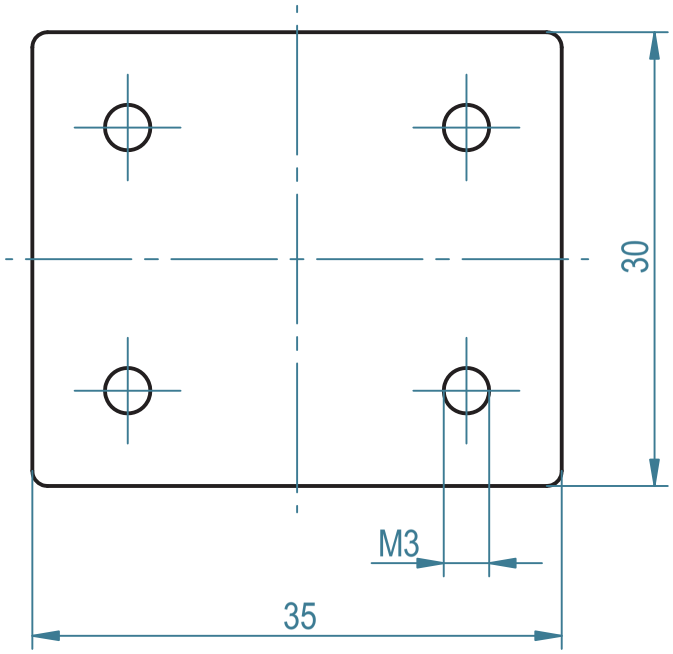


| | NAME | DATE |
|---|---|---|
| DRAWN | Baumgartner | 08/26/09 |
| CHECKED | | |
| ENG APPR | | |
| MGR APPR | | |

UNLESS OTHERWISE SPECIFIED
DIMENSIONS ARE IN MILLIMETERS
ANGLES ±X.X°
2 PL ±X.XX 3 PL ±X.XXX

**SOLID EDGE**
*UGS - The PLM Company*

TITLE: **Contact assembly**

| SIZE | DWG NO | REV |
|---|---|---|
| **A4** | | |

FILE NAME: contact assembly.dft

| SCALE: 2:1 | WEIGHT: | SHEET 1 OF 1 |
|---|---|---|

## 3.3. Construction of the sample tray

The intended sputter deposition (see section 3.4) of silver contacts on the YBCO bars necessitated the construction of a suitable sample tray. Considering the layout of the sputtering chamber, a disc with a diameter of 260 mm is an appropriate basic shape. It was decided that this sample tray should be versatile enough to be used in a wider variety of tasks, and therefore the disc was equipped with circular holes in five different sizes for future applications. Additional five sample positions were designed to accommodate flat samples that can be held in place by 10 mm wide steel bars. These steel bars also served as masks during sputtering, as explained in section 3.4. For this purpose, two holes with a diameter of 1 mm were drilled into each bar at a distance of 5 mm.

The sample tray was designed in Solid Edge and manufactured by the workshop of the institute. Both the disc and the steel bars which hold the samples in place were cut out of a 2 mm thick stainless steel plate. Figure 3.11 shows a three-dimensional view of the sample tray with one of the steel bars attached by two screws. A detailed draft including the dimensions is depicted on page 21. Figure 3.12 shows a photograph of the sample tray after it was mounted in the sputtering machine. Since the sample tray is mounted on a rotary axis inside the sputtering chamber, it can be rotated while sputtering is in progress by turning a knob located underneath the chamber. This allows different samples on the sample tray to be consecutively placed directly above the sputtering source without intermediate opening of the chamber.

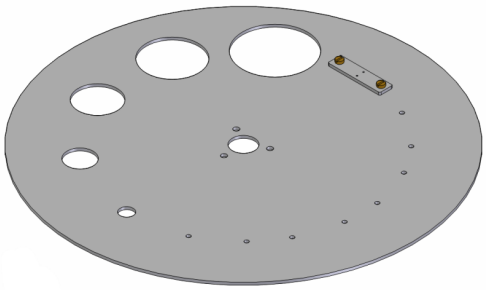

Figure 3.11.: 3D view of the sample tray with one of the steel bars attached.

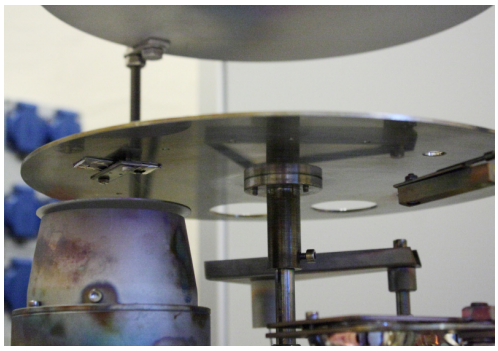

Figure 3.12.: Photograph of the sample tray mounted above the sputtering source (on the left).

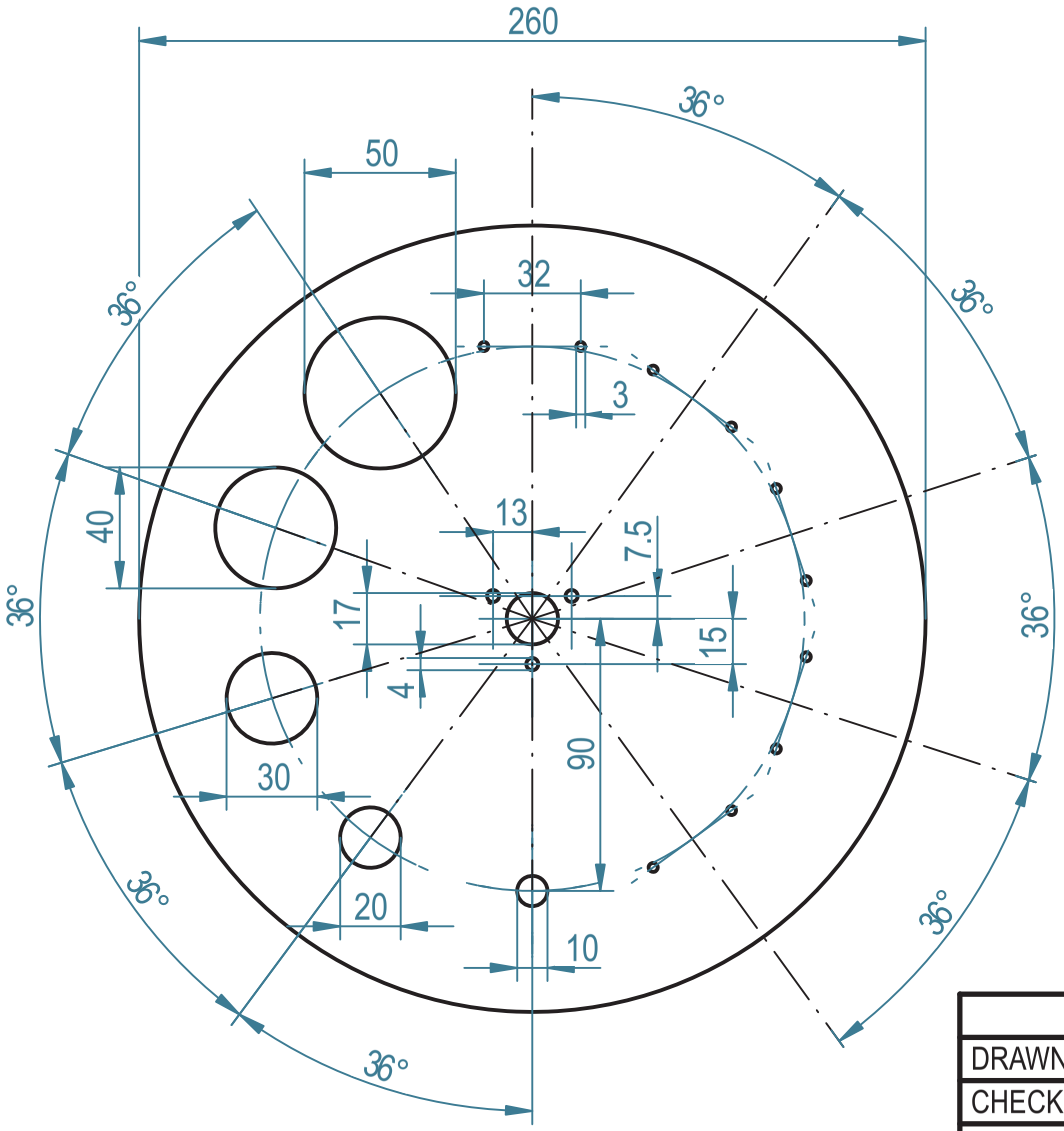


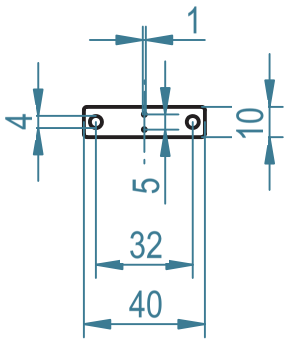


| REVISION HISTORY | | | |
|---|---|---|---|
| REV | DESCRIPTION | DATE | APPROVED |
| | | | |

| | NAME | DATE |
|---|---|---|
| DRAWN | Baumgartner | 08/26/09 |
| CHECKED | | |
| ENG APPR | | |
| MGR APPR | | |

UNLESS OTHERWISE SPECIFIED
DIMENSIONS ARE IN MILLIMETERS
ANGLES ±X.X°
2 PL ±X.XX 3 PL ±X.XXX

**SOLID EDGE**
*UGS - The PLM Company*

TITLE: **Sample tray**

| SIZE | DWG NO | REV |
|---|---|---|
| A4 | | |

FILE NAME: sample tray.dft

| SCALE: 1:2.5 | WEIGHT: | SHEET 1 OF 1 |
|---|---|---|

## 3.4. Sputter deposition of silver contacts

### 3.4.1. Sputtering process

Sputtering is a process in which a solid target is bombarded with ions. These ions cause collision cascades inside the target, which lead to the ejection of atoms, provided the energy of the incident ions is high enough. If the ejected atoms reach a solid object (the so-called substrate), they can bind to its surface, which leads to the deposition of a film of the target material on the substrate. One of the advantages of sputtering over deposition by evaporation is that the target atoms usually exhibit a better adhesion on the substrate because of their higher kinetic energy (approximately 4 eV average impact energy as opposed to 0.2 eV [8]). Detailed information on thin film deposition by means of sputtering can be found in [7].

There are different means by which the ion bombardment can be achieved. The sputtering machine of the institute uses a type ST-20 magnetron sputtering source, manufactured by AJA International. In such a device an electron beam is used to ionize an inert gas (in this case argon) while the magnetic field of several permanent magnets restricts the electrons to helical trajectories close to the target. This ensures a high ion density near the target surface, which results in a high sputter yield. The sputtering source is powered by a type MP-1 magnetron power supply, produced by Advanced Converters. This device is capable of delivering an adjustable DC output voltage within the range $0 \ldots 800$ V and a current of $0 \ldots 2.5$ A. The maximum power output of the power supply is 1 kW.

The MP-1 magnetron power supply allows the user to set the desired sputtering power $P_s$, which is the product of the discharge voltage $U_d$ and the discharge current $I_d$. The discharge voltage depends on $I_d$ and other operational parameters of the sputtering chamber, such as the argon pressure $p_{Ar}$. Lowering this pressure results in a higher discharge voltage at the same power setting. After an extensive testing period (see section 3.4.3), a set of operating parameters suitable for the deposition of silver contacts with a low silver-YBCO contact resistance (see section 3.5.4) was determined. These parameters are listed in section 4.1.1.

The material which was used to deposit contacts on the surface of the samples was a disc-shaped sputtering target with a diameter of two inches, which was obtained from Kurt J. Lesker Company. It consisted of silver with a purity of 99.99% by weight. A thermal membrane (part of the sputtering source) was used to ensure high thermal conductivity between the target and the cathode block of the source in order to prevent unnecessary heating of the target. The procedure used to measure the deposition rate of target material on objects mounted on the sample tray (see section 3.3), is described in section 3.4.2. Since contact resistance measurements

did not indicate a significant correlation between the silver layer thickness and the contact resistance (as expected), contacts with a thickness of 1 µm were produced for the anisotropy measurements described in section 3.7. With the above-mentioned operating parameters the deposition of a 1 µm silver layer requires a sputtering time of 9 min.

The steel bars mentioned in section 3.3 prevented the deposition of silver where it was unwanted, as shown in figures 3.14 and 3.15. The current contacts are deposited above and below the 10 mm wide bar. The two small holes (1 mm in diameter) in the bars are needed for the deposition of the voltage contacts. Since their distance is known (5 mm), a voltage criterion that corresponds to a certain electric field can easily be calculated, as required for the determination of critical currents (see section 3.7). Photographs of the sputtering machine in operation are shown in figures 3.16 and 3.17.

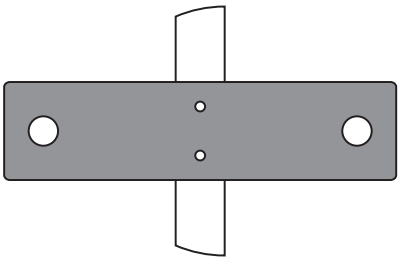

Figure 3.14.: Schematic view of a steel bar masking those areas of a sample where silver deposition is unwanted.

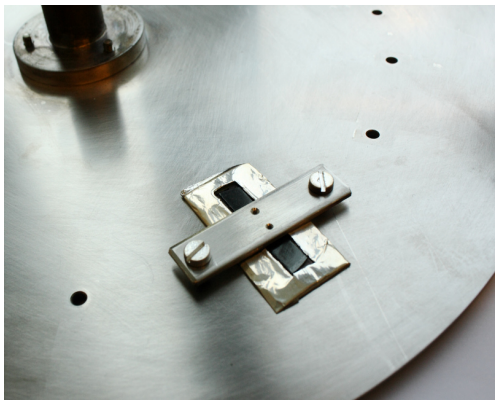

Figure 3.15.: Photograph of a sample mounted on the sample tray. The aluminum foil prevents silver deposition on the epoxy base plate of the sample.

### 3.4.2. Silver deposition rate

In order to know the thickness of the deposited silver contacts, the sputter deposition rate had to be measured. This deposition rate depends on the sputtering source, its operating power, and the target material, which was 99.99% pure silver. According to the ST-20 manual, the deposition rate is approximately proportional to the power the sputtering source is operated at. For this reason, and because a very precise


Figure 3.16.: The sputtering machine in operation. The two tubes are connected to argon and oxygen gas cylinders.

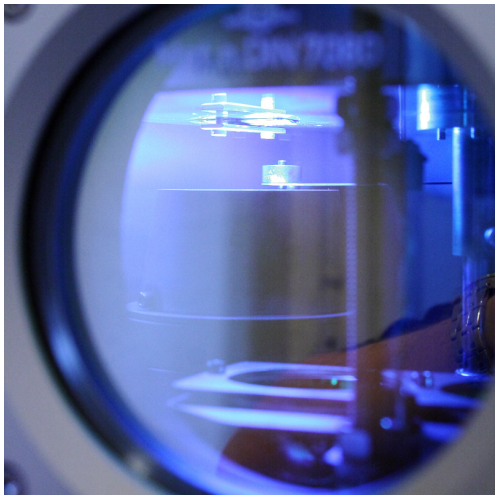

Figure 3.17.: View through the window of the sputtering chamber during the deposition of silver contacts on the surface of sample 0526A.

knowledge of the deposition rate was not needed, it was measured only for one power setting. The following operating parameters were used for the deposition:

Target substrate distance: 77 mm

Argon pressure: $1.0 \cdot 10^{-2}$ mbar

Sputtering power: 78 W

Discharge voltage: 400 V

Five rectangular pieces of aluminum foil with equal masses $m$ were used as substrates. Three of them (A, C, and E in figure 3.18) were consecutively placed directly above the target and sputtered for $T = 10$ min each. The two other pieces (B and D) were situated between these three and were used to measure the indirect deposition rate (deposition on a sample mounted next to the one directly above the target).

The masses of the aluminum substrates were determined with a Sartorius precision balance before they were placed in the sputtering chamber. By measuring the sum of the masses of the A, C, and E foil with the same balance after sputtering, the direct mass deposition rate $\dot{m}_d$ on the surface of each substrate can be calculated

using

$$\dot{m}_d = \frac{m_A + m_C + m_E - 3m}{3T}. \tag{3.1}$$

The indirect mass deposition rate $\dot{m}_i$ is given by

$$\dot{m}_i = \frac{m_B + m_D - 2m}{4T} \tag{3.2}$$

because both substrates were exposed to indirect sputtering from two adjacent substrates. Since the area $A$ of the aluminum foil substrates was known, the direct deposition rate per area and sputtering power is given by

$$d = \frac{\dot{m}_d}{A \cdot P_s}. \tag{3.3}$$

The results of the deposition rate measurement are discussed in section 4.1.2.

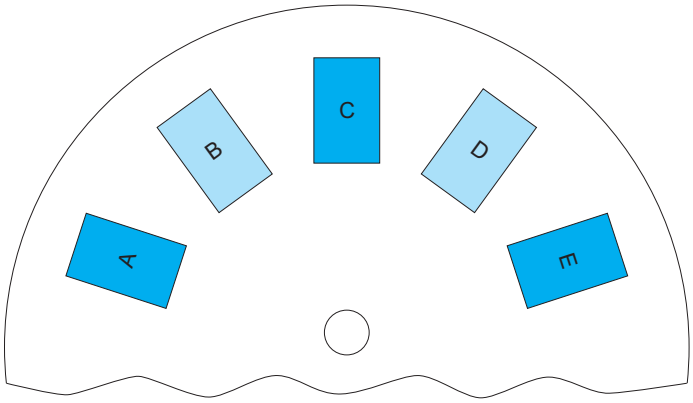


Figure 3.18.: Arrangement of aluminum foil pieces used in the measurement of the deposition rate. The dark ones were placed directly above the source, the bright ones were sputtered indirectly.

### 3.4.3. Determination of suitable sputtering parameters

The sputtering process can be characterized by the following four parameters, which are independent of each other within certain ranges: discharge current $I_d$, argon pressure $p_{Ar}$, target substrate distance $d_{TS}$, and sputtering time $t_s$. The sputtering power $P_s$ is the product of $I_d$ and the discharge voltage $U_d$, which is a function of $I_d$. Therefore, $P_s$ cannot be chosen independently of the other parameters.

The deposition rate shows an inverse square dependence on the distance between the target and the substrate. The geometry of the sputtering chamber and the sample tray made a value of $d_{TS} = 77\,\text{mm}$ convenient. This distance is within the range recommended by the sputtering source manufacturer ($50 \ldots 200\,\text{mm}$), and remained unchanged during all sputtering tests and sample preparation procedures.

At first, the results of the performed sputtering tests seemed to indicate that it is desirable to maximize the discharge voltage. Samples sputtered at a low discharge voltage (around 400 V) exhibited less adhesion of the silver layer than samples sputtered at a high voltage setting (around 700 V). Later it was discovered that the discharge voltage was not responsible for this effect. The poor silver adhesion may have been caused by the higher pressure setting ($1.0 \cdot 10^{-2}\,\text{mbar}$) that was used in the early sputtering attempts. However, the glow discharge cleaning (see section 3.4.4), and the polishing of the sample surfaces prior to sputtering (see section 3.1.2), may also have had an adverse effect on the silver adhesion.

According to [7], high working gas pressures facilitate the development of columnar grains with intercrystalline voids. Since such structures exhibit high electrical resistivity, it appeared sensible to attempt sputtering at the lowest possible pressure setting. A value of $1.3 \cdot 10^{-3}\,\text{mbar}$ was found to be the lowest argon pressure which ensures a stable operation of the sputtering source. Further lowering of the pressure tends to extinguish the glow discharge. Note that the pressure at the time of the plasma ignition is higher (the sputtering source manufacturer recommends $1.0 \cdot 10^{-2}\,\text{mbar}$) and must be decreased afterwards.

Due to the fact that the discharge voltage did not have a significant effect on the silver layer adhesion or the silver-YBCO contact resistance (at least not within the examined range), the sputtering source was operated at a convenient power setting of $P_s = 100\,\text{W}$. At this sputtering power the deposition of a 1 µm silver layer takes 9 min (see section 4.1.2), and $U_d$ is approximately 430 V (assuming $p_{Ar} = 1.3 \cdot 10^{-3}\,\text{mbar}$ and $d_{TS} = 77\,\text{mm}$). A detailed description of the complex dependence of the discharge voltage on the other parameters can be found in [9].

The sputtering time $t_s$ primarily affects the thickness of the deposited layer. Assuming a constant sputtering power, the dependence is linear and the deposition rate is $1.123\,\text{nm}/(\text{W} \cdot \text{min})$, as discussed in section 4.1.2. Depending on the heat conductivity of the system, an increase of $t_s$ may also cause an increase of the substrate temperature. When sputtering YBCO samples, high temperatures may cause oxygen depletion, which has a degrading effect on the superconducting properties of YBCO. However, the aforementioned parameters are unlikely to cause such high substrate temperatures and the experimental results (contact resistance measurements and magnetoscans, see sections 4.2.2 and 4.3) did not indicate the occurrence of oxygen depletion.

The above-mentioned findings are briefly summarized in section 4.1.1. The set of operating parameters for the sputter deposition of silver contacts given in this section will be referred to as standard sputtering parameters henceforth.

### 3.4.4. Glow discharge cleaning

Glow discharge cleaning is a process in which the surface of an electrically conductive object is cleaned by ion bombardment. For this purpose, a glow discharge between the object (cathode) and an auxiliary electrode (anode) is maintained at gas pressures between $10^{-3}$ and $10^{-2}$ mbar. The object and the anode are usually a few centimeters apart, and the applied voltage is typically several hundred volts. The glow discharge causes the surface of the object to be bombarded with positively charged ions at a current density of roughly 100 mA/cm$^2$. This ion bombardment leads to an ablation of material and therefore to a cleaning of the surface.

As a result of the exposure to humidity, YBCO tends to form a non-superconducting surface layer [4]. With the aim of decreasing the silver-YBCO contact resistance by removing this layer, some samples were subjected to glow discharge cleaning, using the built-in cleaning electrode of the sputtering machine. The process was first attempted with argon, since this gas is widely used for glow discharge cleaning, and later with oxygen. The results, which are discussed in section 4.1.3, were similar in both cases: Glow discharge cleaning leads to a drastic increase of the contact resistance of samples subjected to this process.

## 3.5. Contact resistance measurements

The contact resistance, defined as the product of the electrical resistance of a contact and its area,

$$r = R \cdot A, \tag{3.4}$$

was an important property of the manufactured samples because of the high currents that were expected to occur in the anisotropy measurements (see section 4.4). It was initially estimated that the total power dissipation in the contacts of a sample must not exceed the order of 1 W. Assuming an area of 35 mm$^2$ (this value can vary slightly from sample to sample) for each of the two contacts and a current of 100 A (which was a preliminary estimate), a power dissipation of 0.5 W per contact would correspond to a contact resistance of

$$r = R \cdot A = \frac{P}{I^2} \cdot A = \frac{0.5\ \mathrm{W}}{10^4\ \mathrm{A}^2} \cdot 3.5 \cdot 10^{-5}\ \mathrm{m}^2 = 1.75 \cdot 10^{-9}\ \Omega\mathrm{m}^2.$$

This seemed to be a good value to aim for. After a lot of experimentation regarding the sample preparation, contact resistances lower than this value were eventually achieved, as reported in section 4.2.2.

When contacting samples with copper electrodes and indium pads, the total contact resistance can be split into three contributions: the copper-indium contact resistance $r_{Cu-In}$, the indium-silver contact resistance $r_{In-Ag}$, and the silver-YBCO contact resistance $r_{Ag-YBCO}$.

$$r = r_{Cu-In} + r_{In-Ag} + r_{Ag-YBCO} \tag{3.5}$$

The most interesting contribution is $r_{Ag-YBCO}$, since it is the largest of the three values and the only one that can be significantly influenced by the sample preparation. Making the silver-YBCO contact resistance as low as possible was the main objective of the sample preparation process (see sections 3.1 and 3.4).

### 3.5.1. Setup for indium-silver and silver-YBCO contact resistance measurements

The current contacts of the samples consisted of silver layers with 1 µm thickness, whose deposition is described in section 3.4. In all experiments the current was applied through plain copper leads, which were pressed against the sample by screws. Flat pieces of indium were used as mechanical buffers between these copper leads and the silver contacts, since indium is very ductile at room temperature. This ensures that the pressure is distributed evenly throughout the contact area and that the electrical connection is not accidentally limited to a fraction of this area.

The indium was available in the form of a wire, which was rolled until it was sufficiently flat (approximately 0.1 mm). Two pads with a width of roughly 2 mm were cut out of the rolled indium and placed on the current leads of the contact assembly (see section 3.2), as shown in figure 3.20. This procedure was repeated for each of the contact resistance measurements. The pads covered the full width of the leads, and their ends were held in place by small pieces of Kapton tape. The sample was then pressed against the indium pads by the stabilizer plate of the contact assembly, which was screwed down using a preset torque screw driver (see figure 3.21).

The contact assembly was placed in a liquid nitrogen bath in order to reduce the resistance of the sample to zero by cooling it below its critical temperature. A Keithley SourceMeter (model 2601 or 2440) was used to apply a current to the sample, while a Keithley 182 voltmeter measured the voltage drop across the current leads, the indium pads, and the silver contacts on the superconducting sample as shown in figure 3.19 (voltage $U_1$). The voltage between one of the current leads and

the silver contact underneath it (voltage $U_2$) was measured separately by the same voltmeter. For this purpose, a thin copper wire was attached to the silver contact using silver conductive paint. The wire was fed through the hole in the current lead of the contact assembly. Note that the dimensions in the vertical direction (thickness of copper parts, indium pads, and silver contacts) in figure 3.19 are exaggerated for reasons of clarity.

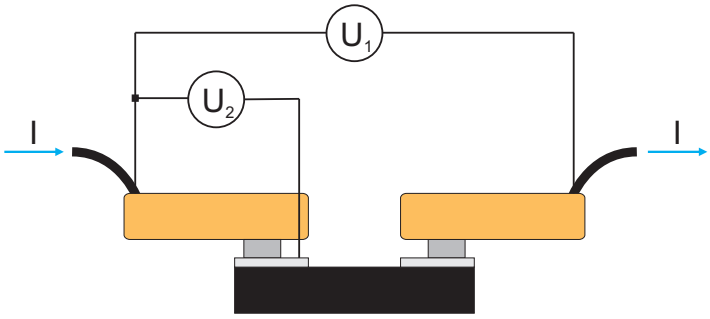


Figure 3.19.: Side view of an YBCO bar (black) with silver contacts (light gray), electrically connected to the current leads (orange) of the contact assembly via indium pads (dark gray).

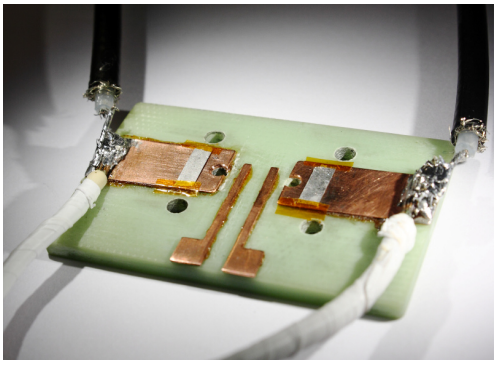

Figure 3.20.: The contact plate of the contact assembly with indium pads on its current leads.

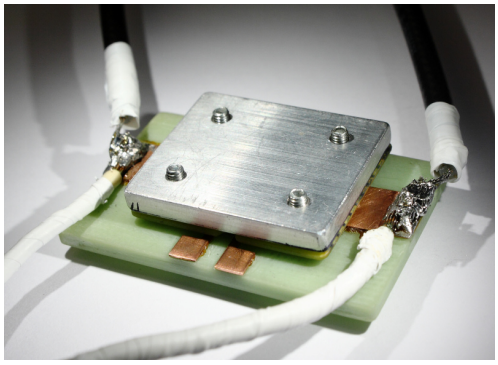

Figure 3.21.: Contact assembly holding a sample between its contact plate and its stabilizer plate.

### 3.5.2. Setup for copper-indium contact resistance measurements

Measuring the copper-indium contact resistance was necessary in order to separate its contribution, as required for the calculations in section 3.5.4. To this end, a copper bar was placed inside the contact assembly instead of an YBCO sample. Just like in the setup for the indium-silver and silver-YBCO contact resistance measurements, electrical contact between the current leads of the contact assembly and the copper bar was established using indium pads. A Keithley 2400 SourceMeter was used to apply the current to the contact assembly and the copper bar.

Since there was only one kind of contact resistance in this setup (copper-indium as opposed to copper-indium, indium-silver and silver-YBCO in the above-mentioned setup), only one voltage had to be measured, which was done by a Keithley 182 voltmeter. The voltmeter was connected to the current leads of the contact assembly, thus measuring the voltage drop across the current leads, the copper bar and the indium pads. The room temperature value of the copper-indium contact resistance was not relevant to the experiments, which is why the contact assembly was cooled to 77 K in a liquid nitrogen bath. Figure 3.22 shows a schematic view of the described setup.

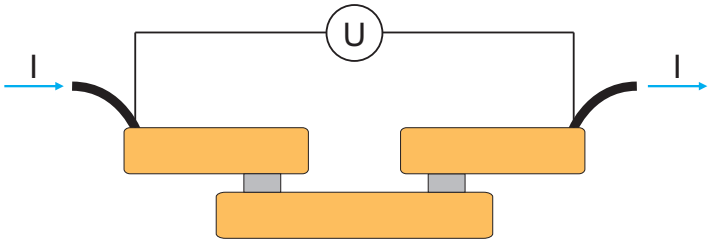


Figure 3.22.: Side view of the current leads (orange) of the contact assembly, the copper bar (orange) and the indium pads (gray).

### 3.5.3. Determination of the pressure dependence

Whenever it was necessary to apply current to a sample, electrical contact was established by pressing copper electrodes against the silver contacts of the sample, with indium pads between them, acting as mechanical buffers. Since YBCO is quite

brittle, it was important to determine the minimum pressure required to provide a sufficiently low contact resistance. Therefore, the pressure dependence[2] of the copper-indium contact resistance was measured. To this end, the contact assembly and a copper bar with the dimensions 30 mm × 10.25 mm × 0.5 mm were used, as explained in section 3.5.2.

Since the copper bar and the current leads had the same cross section $A_{Cu} = 10.25\ \text{mm} \times 0.5\ \text{mm} = 5.125 \cdot 10^{-6}\ \text{m}^2$, the copper resistance can be written as

$$R_{Cu} = \varrho_{Cu(77K)} \cdot \frac{l}{A_{Cu}}, \tag{3.6}$$

where $l = 50$ mm denotes the length of the path the current takes through the copper parts, and $\varrho_{Cu(77K)} = 2.0 \cdot 10^{-9}\ \Omega\text{m}$ [5] is the electrical resistivity[3] of copper at a temperature of 77 K. The contribution of the copper-indium contact resistances is given by

$$R_{Cu-In} = 2\,\frac{r_{Cu-In}}{A_1} + 2\,\frac{r_{Cu-In}}{A_2} = 2\,r_{Cu-In}\left(\frac{1}{A_1} + \frac{1}{A_2}\right), \tag{3.7}$$

where $r_{Cu-In}$ is the copper-indium contact resistance (unit $1\ \Omega\text{m}^2$, as defined in equation (3.4)), and $A_1$ and $A_2$ are the areas of the two indium pads. During all contact resistance measurements (also see section 3.5.4) the areas of the two indium pads were equal within a few per cent. Thus, equation (3.7) can be simplified to

$$R_{Cu-In} = 4\,\frac{r_{Cu-In}}{A_{In}}, \tag{3.8}$$

with $A_{In} = A_1 = A_2$ being the area of one of the indium pads. This area increases with the applied pressure because of the deformation of the indium pads. It was measured with a digital caliper before the copper bar was placed inside the contact assembly, and again after the measurements. The intermediate values were obtained by means of linear interpolation. The resistance of the indium itself can be neglected, since the pads are too thin to produce a relevant contribution. Since the total measured resistance is given by

$$R = R_{Cu} + R_{Cu-In} = \frac{U}{I}, \tag{3.9}$$

where $U$ is the measured voltage and $I$ is the applied current, the copper-indium contact resistance can be expressed as

$$r_{Cu-In} = \frac{A_{In}}{4}\left(R - \varrho_{Cu(77K)}\,\frac{l}{A_{Cu}}\right). \tag{3.10}$$

[2] Actually the dependence on the setting of a preset torque screwdriver was measured. Knowing the corresponding contact pressure was not necessary to ensure reproducibility.

[3] The value actually depends on the purity of the copper, which was unknown in this case. However, the purity dependence of the electrical resistivity is not very pronounced at this temperature.

$R$ was measured for six different torque settings using a current of 1 A, and $r_{Cu-In}$ was calculated using (3.10). After each measurement, the contact assembly was removed from the liquid nitrogen bath and warmed up to room temperature using a heat gun. The contact pressure was then increased by adjusting the setting of the preset torque screw driver and tightening the screws with the new setting. The results of the measurements are given in section 4.2.1.

### 3.5.4. Determination of indium-silver and silver-YBCO contact resistances

The procedure used to measure the indium-silver (between the indium pads and the current contacts of the sample) and the silver-YBCO (between the sputtered silver contacts and the superconductor) contact resistances is described in detail in section 3.5.1. In most contact resistance measurements, the indium pads used to establish electrical contact between the current leads of the contact assembly and the sample did not cover the contact areas of the sample completely. Since the screws of the contact assembly were tightened using the same torque (0.09 Nm) which was used for the screws of the sample holders in the anisotropy measurements (in which case the indium pads covered the current contacts of the sample completely), the resulting contact pressure was higher in the contact assembly. However, the copper-indium contact resistance $r_{Cu-In}$ was virtually the same because of the saturation found in the pressure dependence of the contact resistance (see figure 4.2). As pointed out in section 3.5.2, $r_{Cu-In}$ had to be known in order to calculate $r_{In-Ag}$ and $r_{Ag-YBCO}$. For the calculations in this section its value was assumed to be

$$r_{Cu-In} = 3 \cdot 10^{-10}\ \Omega\mathrm{m}^2,$$

in accordance with the results discussed in section 4.2.1. During the measurements, a current was applied to the samples using the contact assembly, and the voltage $U_1$ between the current leads was measured as depicted in figure 3.19. The voltage $U_2$ between one of the current leads and the silver contact underneath it, which is necessary to separate the indium-silver contribution, was not measured in all cases, since the total contact resistance was the more interesting value from an experimental point of view. Let $I$ be the applied current. Since $I$ is known, the two resistances

$$R_1 = \frac{U_1}{I}, \qquad R_2 = \frac{U_2}{I} \tag{3.11}$$

can be calculated. With $l$ being the length of the path the current takes through the current leads, which was measured by determining the positions of the indium pads using a digital caliper, the resistance contribution of the copper current leads can be expressed as

$$R_{Cu} = \varrho_{Cu(77K)} \cdot \frac{l}{A_{Cu}}. \tag{3.12}$$

$A_{Cu} = 5.125 \cdot 10^{-6}$ m$^2$ is the cross section of the current leads, and $\varrho_{Cu(77K)}$ is once again assumed to be $2.0 \cdot 10^{-9}$ Ωm. Since the areas of the two indium pads were identical within a few per cent, the copper-indium contribution is given by (see section 3.5.3)

$$R_{Cu-In} = 2\,\frac{r_{Cu-In}}{A_{In}}, \tag{3.13}$$

where $A_{In}$ is the area of one of the indium pads. Similar expressions describe the indium-silver and the silver-YBCO contact resistance contributions:

$$R_{In-Ag} = 2\,\frac{r_{In-Ag}}{A_{In}} \tag{3.14}$$

$$R_{Ag-YBCO} = 2\,\frac{r_{Ag-YBCO}}{A_{In}} \tag{3.15}$$

Using these contributions, the resistances $R_1$ and $R_2$ can be written as

$$R_1 = R_{Cu} + R_{Cu-In} + R_{In-Ag} + R_{Ag-YBCO}, \tag{3.16}$$

and

$$R_2 = \frac{1}{2}\,(R_{Cu} + R_{Cu-In} + R_{In-Ag})\,. \tag{3.17}$$

The factor $\frac{1}{2}$ in equation (3.17) considers that the current flows through only one current lead and one indium pad in this case (see figure 3.19). Since $r_{Cu-In}$ is known, $R_{Cu-In}$ can be calculated. Thus, rearranging (3.17) to

$$R_{In-Ag} = 2\,R_2 - R_{Cu} - R_{Cu-In} \tag{3.18}$$

allows to calculate the indium-silver contribution. Using (3.14) and (3.18), one finds the indium-silver contact resistance:

$$r_{In-Ag} = A_{In}\left(R_2 - \frac{R_{Cu}}{2} - \frac{R_{Cu-In}}{2}\right). \tag{3.19}$$

Rearranging (3.16) and substituting $R_{In-Ag}$ by the expression in (3.18), yields the silver-YBCO contribution:

$$R_{Ag-YBCO} = R_1 - 2\,R_2 \tag{3.20}$$

With equation (3.15) the silver-YBCO contact resistance can be expressed as

$$r_{Ag-YBCO} = A_{In}\left(\frac{R_1}{2} - R_2\right). \tag{3.21}$$

The total contact resistance

$$r = r_{Cu-In} + r_{In-Ag} + r_{Ag-YBCO} \tag{3.22}$$

can also be calculated from (3.16) using

$$r = \frac{A_{In}}{2} \left(R_1 - R_{Cu}\right), \tag{3.23}$$

in case $R_2$ was not measured.

The results of these measurements are contained in table 4.1 in section 4.2.2. Substituting the measured resistances into the above-mentioned equations does in some cases result in negative values of $r_{In-Ag}$, whose absolute values are small compared to the total contact resistance $r$. This can be explained as follows: The indium-silver contact resistance is very low, which means the difference between $R_2$ and $R_{Cu}/2$ in (3.19) is small compared to their absolute values. Therefore, a small inaccuracy of the calculated value $R_{Cu}$ (more precisely: the length $l$ of the path of the current in (3.12)) can result in negative values of $r_{In-Ag}$. As a consequence of the low indium-silver contact resistance, the approximation

$$r \approx r_{Cu-In} + r_{Ag-YBCO} \tag{3.24}$$

can be used. Based on this approximation, the silver-YBCO contact resistances listed in table 4.2 were calculated by subtracting $r_{Cu-In}$ from $r$, whose value was obtained using (3.23).

## 3.6. Magnetoscans

The magnetoscan technique (detailed information can be found in [10]) uses a permanent magnet to induce currents in a superconducting sample by moving this magnet across the surface of the sample. Magnetic fields that are generated by these currents inside the superconductor are measured by a Hall probe, which is attached to the scanning head. The sample (whose critical temperature must be above 77 K) as well as the scanning head are immersed in liquid nitrogen during the scan. The Hall probe used for the magnetoscans that were performed on some of the samples has a sensitivity of 99.32 mV/T, and its Hall voltage was measured with a Keithley 2700 voltmeter. This voltmeter was connected to a computer which recorded the magnetic field and the coordinates of each point of the scanning raster, thereby mapping the magnetization of the sample. For all performed scans the scanning head was placed directly above (approximately 50 µm distance) the sample surface and a spatial resolution between 0.1 mm and 0.2 mm was chosen.

Magnetoscans allow the detection of non-superconducting domains such as Y-211 inclusions, thermally or chemically damaged regions, and cracks within a sample. An estimation of the critical current density based on the measured magnetization and the cross section of the sample is also possible. Figures 3.23 and 3.24 show the head of the magnetoscanner scanning across the surface of sample 0731A. The magnetoscan maps shown in section 4.3 depict the spatial distribution of the magnetization of the respective sample, which was achieved by color coding the output of the Hall probe. An appropriate offset was chosen in order to map the original data to an interval of $0 \ldots 15$ mT by subtracting the background value caused by the permanent magnet.

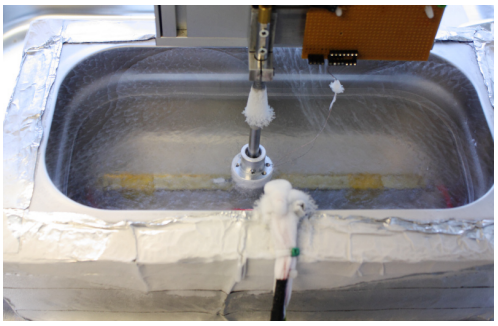

Figure 3.23.: Sample 0731A (immersed in liquid nitrogen) in the magnetoscanner.

Figure 3.24.: Close-up picture of the head of the magnetoscanner during a scan.

## 3.7. Anisotropy measurements

An anisotropy measurement – as the term is used in the thesis at hand – determines the angular dependence of the critical current of a sample in an external magnetic field. This is achieved by stepwise variation of the angle between the $ab$-plane of the sample (which is parallel to the surface with the silver contacts) and the magnetic field vector, as depicted in figure 3.25. For each angle the transport current, which flows through the superconducting sample parallel to its $ab$-plane, is ramped up until a transition to the dissipative state is detected. In this way, the critical current for this particular angle, magnetic field, and temperature can be determined.

The evaluation of the raw data was done with Scilab 4[4], using a critical current evaluation function written by Florian Hengstberger. This function computes $I_c$

[4]Scilab is a scientific software package for numerical computations.

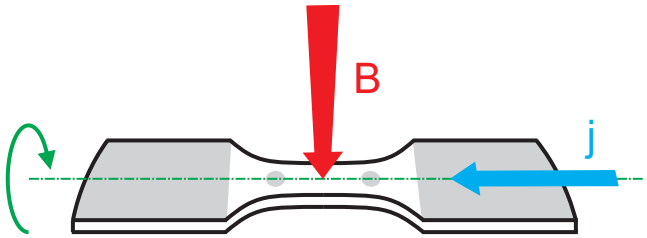


Figure 3.25.: By rotating either the sample or the field as indicated by the green arrow, the angle between the $ab$-plane and the magnetic field can be varied.

for each voltage-current curve by intersecting a linear interpolation of the measured voltage values with a voltage criterion $U_c$, which must be defined by the user. The plots presented in sections 4.4.1 and 4.4.2, contain the critical current densities $J_c$ instead of the critical currents. The $J_c$ values were calculated by dividing $I_c$ by the apparent cross section of the sample:

$$J_c = \frac{I_c}{A_{app}} \tag{3.25}$$

Note that $A_{app}$ was obtained by measuring the outer dimensions of the samples with a digital caliper, whereas the effective cross section $A_{eff}$ may be smaller due to material defects such as Y-211 inclusions and cracks. The two setups that were used for the anisotropy measurements presented in section 4.4 are described in the following.

### 3.7.1. Electromagnet system

A water-cooled electromagnet was used for anisotropy measurements up to a magnetic field of 1.4 T. A Dewar was placed between its pole shoes, which allows a sample to be immersed in liquid nitrogen. For that purpose, the sample is mounted on a sample rod, which is then inserted into the liquid nitrogen and held in place by screwing it to a metal stand. An electric motor allows the magnet to be rotated around the sample rod, thereby changing the angle between the field and the $ab$-plane of the sample.

The sample rod was designed to apply a current to a sample by connecting it to a computer-controlled Heinzinger TNSUs 10-300 current source. It also allowed to measure the voltage between the voltage contacts of the sample by connecting them

to a Keithley 182 voltmeter. Electrical contact between the current contacts of the sample and the copper electrodes of the sample holder (anterior part of the rod) was established by coating the contact areas with indium (approximately 0.1 mm thick, see figure 3.26) and pressing the electrodes against the sample by tightening four screws with a preset torque screw driver. Electrical contact between the voltage contacts and the wires that led to the voltmeter was established with silver conductive paint as shown in figure 3.27.

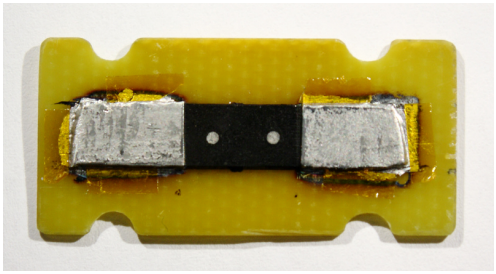

Figure 3.26.: Sample with indium coating on its current contacts.

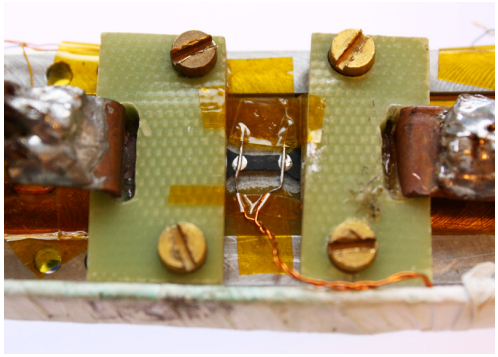

Figure 3.27.: Sample mounted in the sample holder of the rod belonging to the electromagnet. The two wires connect the voltage contacts to a voltmeter.

After giving the silver paint sufficient time to dry, the sample rod can be inserted into the Dewar. A mark on the rod helps positioning it so that the sample is located between the pole shoes, where the magnetic field is homogeneous. It is noteworthy that one of the samples cracked during cooling in liquid nitrogen (see figure 3.28). Since the sample rod was inserted very slowly in this case, the crack may have been the result of a high temperature gradient. In the subsequent measurements the sample rod was inserted more quickly, which certainly lead to a more homogeneous cooling of the rod itself and the sample it held, thus reducing the temperature gradient.

Once the sample rod is inserted into the Dewar, and the connections to the current source and the voltmeter are established, the measurement can commence. A software designed for this specific task controls the current source and the field of the magnet as well as its rotation, while saving the readings of the voltmeter to files. The user must specify the desired magnetic field, the range of the rotation angle, the angular step size, the current ramp rate, the maximum allowed current and the voltage criterion. The latter is the value of the voltage between the voltage contacts,

at which the ramping of the current stops (unless the maximum allowed current is reached before that). Once the parameters have been set, the measurement is carried out automatically by the software.

While the measurement is in progress, the software records one voltage-current curve for each angular step within the specified range and stores the data in a file. After the measurement is completed, the data in these files can be analyzed by another software that determines the critical current for each of these voltage-current curves. Plotting the critical current (density) as a function of the angle between the *ab*-plane of the sample and the magnetic field vector, yields a so-called anisotropy curve. The results of the anisotropy measurements in the electromagnet can be found in section 4.4.1. Figure 3.29 shows a photograph of the electromagnet in operation.

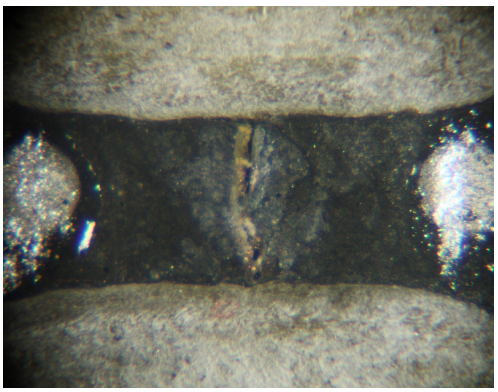

Figure 3.28.: The bridge of sample 0625B cracked during cooling.

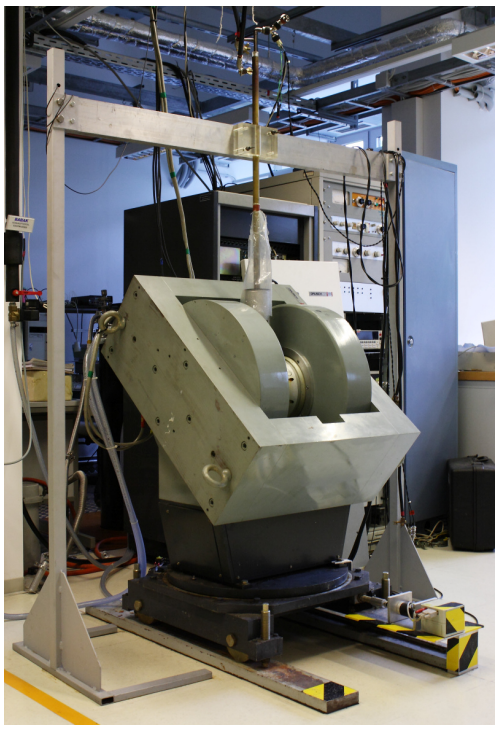

Figure 3.29.: The 1.4 T electromagnet in operation.

### 3.7.2. Superconducting 6 T magnet system

While the principle was the same as in the electromagnet setup described above, the measurements with the superconducting magnet were performed in a cryostat that uses helium gas flow cooling. By creating a control loop consisting of a temperature sensor which is mounted inside the sample space, and the heater of the cryostat, the sample temperature can be regulated within a wide range. The superconducting magnet is able to provide a maximum field of 6 T.

Again, the sample was mounted in the sample holder of a sample rod and contacted with indium pads (current contacts) and silver conductive paint (voltage contacts), as described in section 3.7.1. However, a different sample rod had to be used, since the superconducting magnet cannot be rotated around the sample, which means the rod itself had to be rotated by means of an electric motor. The sample holder of this rod could not accommodate the same sample width as the one used in the electromagnet. As a consequence, the epoxy base plates of the samples had to be cut prior to mounting them on the sample rod. A photograph of the sample holder belonging to the superconducting magnet is shown in figure 3.30.

After inserting the sample rod into the cryostat and making the necessary electrical connections, the system cools the sample and stabilizes the temperature at a user-defined value. The bridge of sample 0720A was severely damaged during cooling, which probably happened due to mechanical stress caused by the temperature gradient. When the measurements were repeated with sample 0731A, the cooling rate was reduced to 0.5 K/min in order to spare this sample the fate of its predecessor. Once the temperature set point is reached and the temperature is stable, the measurements can commence. Since the system is computer-controlled, all scheduled measurements (including changes of the temperature set point, magnetic field, etc.) can be programmed into a sequence file, which is then executed command by command.

During an anisotropy measurement, a voltage-current curve is recorded for each angular step, just like in the electromagnet measurements. The data of the measurement is stored in a file, which can be analyzed later. This file also contains the output voltage of a Hall probe, which is mounted on the sample rod. It can be used to determine the $H \,||\, ab$ direction (minimum of the Hall voltage) when evaluating the data. Section 4.4.2 contains the results of the anisotropy measurements performed with the 6 T superconducting magnet system. A photograph of the cryostat and the connected devices is shown in figure 3.31.

Figure 3.30.: Sample holder of the 6 T superconducting magnet, holding sample 0731A.

Figure 3.31.: Cryostat containing the superconducting magnet, and a rack full of equipment required to operate it.

## 3.8. List of samples

This section is aimed at providing a better understanding of the progression of the sample preparation process and the measurements. For this purpose, all samples that were manufactured are listed in chronological order in the following, accompanied by a short description.

### Sample 0318A

This very first sample was a 0.2 mm thick YBCO disc that had been cut from a bulk cylinder by another person before I began my sample preparation work. Sample 0318A was used for testing glow discharge cleaning in argon and sputtering. Contact resistance measurements were not possible with this sample, since its faces were not sufficiently plane-parallel to mount it into the contact assembly (see section 3.2). Sample 0318A also served to demonstrate that mounting the YBCO disc on an epoxy plate using low temperature varnish, and then cooling it with liquid nitrogen, does not cause the formation of cracks.

### Sample 0402A

This was the first sample which was produced using the mechanical preparation method described in section 3.1. The YBCO bar of sample 0402A was 1.1 mm thick and the sample was used to determine an appropriate grit number for the grinding process. Glow discharge cleaning in an argon atmosphere was also tested with this sample. During an attempt to determine the indium-YBCO contact resistance[5] using the contact assembly, the sample cracked. Its surface was probably not plane enough, which resulted in a non-uniform distribution of the mechanical stress when the screws were tightened.

### Copper sample

A copper bar with the dimensions 30 mm × 10.25 mm × 0.5 mm was manufactured for the copper-indium contact resistance measurements discussed in sections 3.5.2 and 3.5.3. It was cut from the same material that was used for producing the current leads of the contact assembly.

[5] Placing indium pads directly on the surface of the superconductor instead of depositing silver contacts first, results in much higher contact resistance values.

### Sample 0424A

The YBCO bar of sample 0424A was from the same disc as the one used in the production of sample 0402A. This sample was used for testing different sputtering parameters and glow discharge cleaning in argon as well as in oxygen. Due to repeated grinding (to remove the old silver layer before sputtering again), the thickness of the sample was reduced from originally 1.1 mm to 0.85 mm over the course of several weeks. After mounting sample 0424A into the electromagnet system (see section 3.7.1), transitions to the dissipative state were discovered at unexpectedly low transport currents and magnetic fields of 1.4 T and 0.5 T respectively. This behavior called for an anisotropy measurement, which was performed at a field of 1 T. However, the results of this measurement were inconclusive and it was later discovered that the sample had cracked (probably when tightening the screws or during cooling).

### Sample 0526A

Sample 0524A was cut from a 0.4 mm thick YBCO disc. Soldering a wire to one of the sputtered current contacts instead of using silver conductive paint to establish an electrical connection was tested with this sample. Magnetoscans (see sections 3.6 and 4.3), which were performed before and after soldering, revealed that the local temperature increase during soldering damages the sample.

### Sample 0609A

This sample was cut from the same disc as sample 0526A. It was used to test the effect of carving grooves into its surface prior to sputtering. Sample 0609A was measured with the electromagnet system and exhibited an unexpectedly low critical current. This circumstance facilitated the first successful anisotropy measurement at a magnetic field of 1.4 T and a temperature of 77 K. After the measurement a crack perpendicular to the direction of the current was found in the sample, which could explain the low critical current.

### Sample 0625A

With a thickness of only 0.2 mm, the YBCO disc used to produce this sample was the thinnest that had ever been cut from the bulk cylinder. During measurements in the electromagnet, the measured voltage exhibited an unusual dependence on the transport current. A crack which might have been responsible for the observed behavior was discovered after removing sample 0625A from the sample rod.

### Sample 0625B

Sample 0625B was cut from the same 0.2 mm YBCO disc as sample 0625A. It was the first sample whose silver contacts were deposited using the sputtering parameters listed in section 4.1.1 (higher discharge voltages and shorter sputtering times had been used for the previously manufactured samples). Sample 0625B was also the first sample which was milled in order to reduce its cross section. However, the bridge of the sample cracked when it was cooled with liquid nitrogen in an attempt to perform measurements with the electromagnet system.

### Sample 0703A

This sample was cut from a 0.5 mm thick YBCO disc. After a bridge was milled into the sample, it was measured in the electromagnet. The bridge cracked while the magnet was rotated in order to change the field orientation from $H \,||\, c$ to $H \,||\, ab$ (see figure 3.32). This crack may have been caused by the $\vec{M} \times \vec{B}$ torque resulting from the magnetization of the sample.

### Sample 0703B

Sample 0703B was cut from the same disc as sample 0703A and went through exactly the same preparation processes. The fact that in the end its silver-YBCO contact resistance was approximately three times that of sample 0703A, was the first solid indication for a contact resistance dependence on material defects (which can be distributed inhomogeneously throughout the bulk cylinder). With the aim of attaining a lower contact resistance by sputtering again, the silver layer of sample 0703B was removed and new grooves were carved into its surface. Unfortunately, the sample cracked during this process.

### Sample 0720A

This sample was produced using a 0.45 mm thick YBCO bar. Contact resistance measurements on this sample indicated that carving grooves into the surface significantly reduces the silver-YBCO contact resistance. A bridge was milled into the sample and it was measured in the electromagnet. Sample 0720A showed a behavior very similar to that of sample 0609A: The critical current was much lower than expected. Anisotropy measurements at 1 T and 0.5 T were successfully performed. A subsequent magnetoscan revealed a very inhomogeneous magnetization of the sample, most likely caused by a large number of inclusions, which could also explain the low critical current. The sample was destroyed in an attempt to measure its transport current anisotropy using the 6 T superconducting magnet (see section 3.7.2) as shown in figure 3.33.

### Sample 0720B

The YBCO bar of this sample was cut from the same disc as the bar of sample 0720A. Even though sample 0720A and 0720B had received exactly the same treatment, the latter exhibited two times the silver-YBCO contact resistance of its twin. In an attempt to reduce the contact resistance, the sample was ground, carved, and sputtered again. However, only an insignificant decrease of the contact resistance was achieved. A bridge was milled into sample 0720B before it was measured in the electromagnet. During a zero field measurement the sample was destroyed at a transport current of 135 A, which allowed the calculation of the maximum acceptable power dissipation in the current contacts, in case of liquid nitrogen cooling. The result was 1 W per contact, i. e. 2 W total power dissipation.

### Sample 0728A

Sample 0728A was cut from the bottommost part of the bulk cylinder and was 0.25 mm thick. The silver-YBCO contact resistance of this sample was extremely high (approximately 50 times the expected value), which was most likely caused by inclusions of the Y-211 phase. An anisotropy measurement was out of the question due to the high contact resistance.

### Sample 0728B

This sample was cut from the same disc as sample 0728A, which explains why the two samples exhibited a similarly high contact resistance. A magnetoscan was performed on sample 0728B, which revealed a very inhomogeneous magnetization. This result also points to a large number of Y-211 inclusions.

### Sample 0731A

Sample 0731A was produced using a 0.7 mm thick YBCO disc which had been cut from the bulk cylinder prior to the production of the above-mentioned samples. Since this disc stemmed from the top of the cylinder, it contained considerably less inclusions than the one used in the production of samples 0728A and 0728B. After measuring an excellent contact resistance, a bridge was milled into the sample. Anisotropy measurements at different magnetic fields were successfully performed with this sample in the superconducting magnet system (see section 4.4.2).

### Sample 0731B

This sample was cut from the same top layer YBCO disc as sample 0731A, and the two samples were sputtered together. However, the silver-YBCO contact resistance was approximately twice as high as that of sample 0731A. This may have been caused by the shorter grinding time of sample 0731B (10 min as opposed to 30 min).

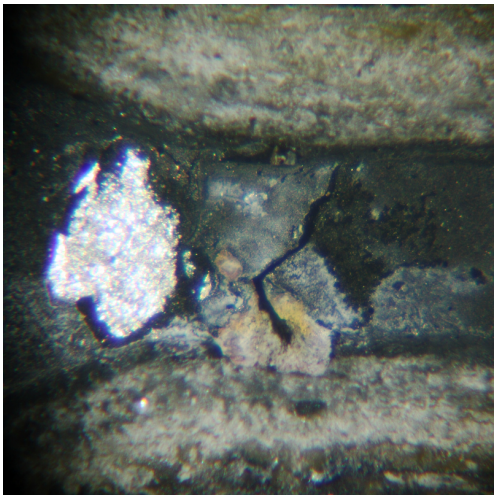

Figure 3.32.: Sample 0703A cracked during measurements in the electromagnet.

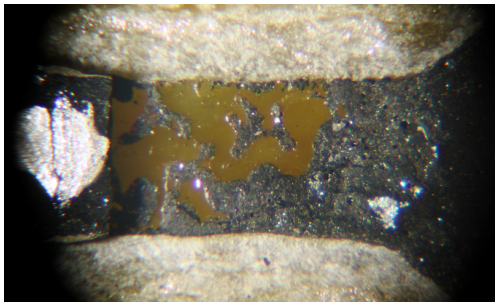

Figure 3.33.: The bridge of sample 0720A was destroyed during cooling in the helium gas flow cryostat.

# 4. Results

## 4.1. Sputtering

The experimental results which are connected to the sputter deposition of silver contacts on the sample surfaces are discussed in the following.

### 4.1.1. Standard sputtering parameters

The empirical determination of sputtering parameters suitable for sample preparation is described in section 3.4.3. To summarize the findings of that section, the following sputtering parameters are suitable for the deposition of a 1 µm thick silver layer on YBCO samples and are therefore referred to as standard sputtering parameters:

Target substrate distance: $d_{TS} = 77$ mm

Argon pressure: $p_{Ar} = 1.3 \cdot 10^{-3}$ mbar

Sputtering power: $P_s = 100$ W

Discharge voltage: $U_d \approx 430$ V (function of other parameters)

Sputtering time: $t_s = 9$ min

### 4.1.2. Silver deposition rate

The procedure used for measuring the silver deposition rate of the sputtering machine is described in section 3.4.2. The results of the mass measurements mentioned in that section were

$$m = 28.69 \text{ mg}, \qquad m_A + m_C + m_E = 106.74 \text{ mg}, \qquad m_B + m_D = 59.62 \text{ mg}.$$

Substituting these values into the equations (3.1) and (3.2) yields

$$\dot{m}_d = 0.689 \text{ mg/min}, \qquad \dot{m}_i = 0.056 \text{ mg/min}$$

for the operating parameters given in section 4.1.1. The indirect deposition rate on an adjacent substrate is approximately 8% of the direct deposition rate. If several samples are sputtered at once, and the layer thickness is a critical parameter, this indirect deposition obviously has to be taken into account. With the area of each aluminum foil substrate exposed to sputtering being $A = 7.5 \text{ cm}^2$ , the direct deposition rate per area and sputtering power can be calculated using equation (3.3):

$$d = 1.178 \frac{\mu\text{g}}{\text{cm}^2 \cdot \text{W} \cdot \text{min}}. \tag{4.1}$$

The unit of $d$ in equation (4.1) was chosen because it is more convenient than the SI unit 1 $\text{kg}/(\text{m}^2 \cdot \text{W} \cdot \text{s})$. With the density of silver, which is 10.49 $\text{g/cm}^3$, one finds that this result corresponds to a silver layer growth rate of 1.123 $\text{nm}/(\text{W} \cdot \text{min})$.

### 4.1.3. Influence of glow discharge cleaning

Glow discharge cleaning (see section 3.4.4) of samples prior to sputtering was attempted with argon as well as oxygen. The results of these attempts are given in the following.

#### Glow discharge cleaning in argon

The samples were mounted on the sample tray (see section 3.3) at a distance of 30 mm from the anode, and the following two sets of operating parameters were tested:

Voltage: $U = 700 \text{ V}_{\text{DC}}$

Argon pressure: $p_{Ar} = 7 \cdot 10^{-2}$ mbar

Cleaning time: $t$ =5 min

$U = 850 \text{ V}_{\text{DC}}$

$p_{Ar} = 7 \cdot 10^{-2}$ mbar

$t$ =30 s

The resulting discharge current was within the range 20 . . . 45 mA and fluctuated considerably during the process. After the glow discharge cleaning was completed, silver contacts were applied to the samples by means of sputtering (see section 3.4). The sputtering chamber was not flooded with air between the two processes in order to avoid contamination of the sample surfaces. Contact resistance measurements (see section 3.5.4) revealed an unexpected result: The contact resistances of the samples were of the order of $10^{-5}$ $\Omega m^2$ – clearly far too high, considering that this would correspond to a resistance of approximately 0.3 Ω for a typical sample contact with an area of 35 $mm^2$.

### Glow discharge cleaning in oxygen

An unacceptably high oxygen deficiency of the samples caused by the temperature increase during glow discharge cleaning was considered a possible cause of the observed high contact resistance. In order to counteract this potential problem, glow discharge cleaning in an oxygen atmosphere was attempted with the following sets of operating parameters:

$U = 2100\ V_{DC}$

$p_{O_2} = 10^{-2}$ mbar

$t$ =40 min

$U = 2000\ V_{AC}$

$p_{O_2} = 10^{-2}$ mbar

$t$ =40 min

$U = 550\ V_{DC}$

$p_{O_2} = 0.1$ mbar

$t$ =30 min

The results were similar to those obtained with argon: The contact resistances were much too high. Therefore, glow discharge cleaning was omitted in all subsequent sample preparation procedures. It is noteworthy that samples which had undergone glow discharge cleaning, showed a non-ohmic behavior in the contact resistance

measurements. The resistance-current curves of sample 0424A, which were measured after two consecutive sputtering attempts with prior glow discharge cleaning, are depicted in figure 4.1. Clearly the behavior was not only non-ohmic but also qualitatively different for the two measurements. Since glow discharge cleaning was not pursued further, this phenomenon remained uninvestigated.

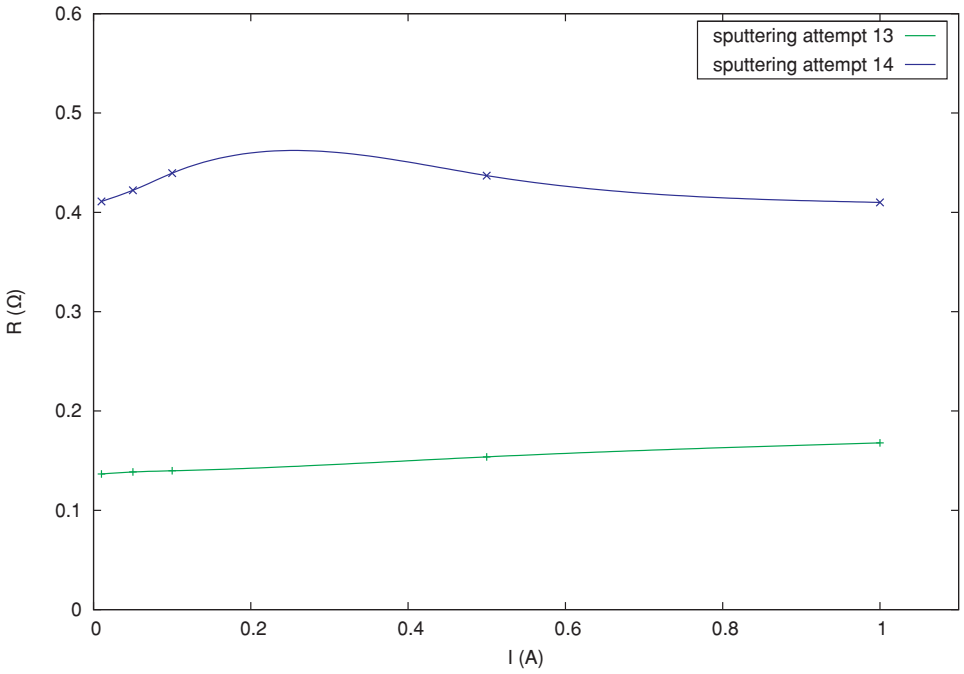


Figure 4.1.: Non-ohmic behavior after glow discharge cleaning (the lines are spline interpolations). The current dependence of the resistance of sample 0424A was qualitatively different after two consecutive sputtering attempts.

## 4.2. Contact resistances

### 4.2.1. Influence of the contact pressure

The method used to determine how pressure exerted by the screws of the pressure contacts affects the copper-indium contact resistance, is described in section 3.5.3. The contact resistance did not show a pronounced pressure dependence, and it exhibited a saturation effect at a relatively low torque setting, as shown in figure 4.2. The experience with the samples 0424A, 0609A, and 0625A (see section 3.8)

indicated that a torque setting of 0.17 Nm (which seemed to be convenient at the time) may cause mechanical damage when the sample is mounted on a sample rod in preparation for an anisotropy measurement. Therefore, a new torque setting of 0.09 Nm was chosen and used for tightening the screws of the contact assembly and the sample holders of the sample rods in all subsequent contact resistance and anisotropy measurements. The corresponding copper-indium contact resistance is approximately $3 \cdot 10^{-10}\ \Omega\mathrm{m}^2$, assuming conditions similar to those in the copper-indium contact resistance measurement (four M3 screws with a pitch of 0.55 mm and indium pads with $A_{In} \approx 25\ \mathrm{mm}^2$).

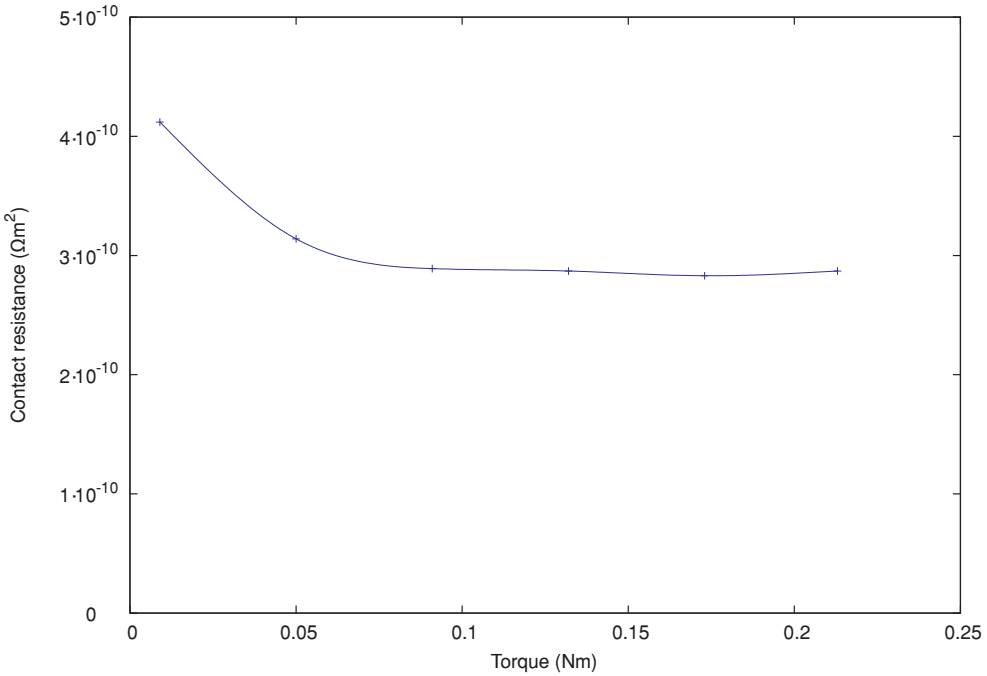


Figure 4.2.: Torque dependence (preset torque screw driver) of the copper-indium contact resistance at 77 K. Obviously the contact resistance goes into saturation at a relatively low contact pressure.

### 4.2.2. Indium-silver and silver-YBCO contact resistances

Table 4.1 contains the results of the indium-silver and silver-YBCO contact resistance measurements described in section 3.5.4. Each row represents the best result (i. e. the lowest total contact resistance) for a particular sample. The number in brackets next to the sample name is the sputtering attempt after which the corresponding measurement was performed. Two extra rows (0424A (18) and 0609A (02))

were added in order to demonstrate the effects of different preparation procedures on the same sample. The resistances presented in table 4.1 are averaged over at least[1] three values measured at different currents which ranged from 10 mA to 1 A. This was done to check for non-ohmic behavior, which was found in samples that had undergone glow discharge cleaning (see section 4.1.3).

| **Sample** | **l (m)** | $\mathbf{A_{In}\ (m^2)}$ | $\mathbf{R_1\ (\Omega)}$ | $\mathbf{R_2\ (\Omega)}$ |
|---|---|---|---|---|
| 0424A (05) | 0.030 | $1.33 \cdot 10^{-5}$ | $2.449 \cdot 10^{-4}$ | – |
| 0424A (18) | 0.031 | $1.47 \cdot 10^{-5}$ | $7.441 \cdot 10^{-2}$ | – |
| 0526A (03) | 0.030 | $1.45 \cdot 10^{-5}$ | $1.779 \cdot 10^{-3}$ | – |
| 0609A (02) | 0.030 | $1.43 \cdot 10^{-5}$ | $3.971 \cdot 10^{-4}$ | $2.221 \cdot 10^{-5}$ |
| 0609A (04) | 0.030 | $1.31 \cdot 10^{-5}$ | $8.792 \cdot 10^{-5}$ | $3.599 \cdot 10^{-5}$ |
| 0625A (01) | 0.032 | $1.32 \cdot 10^{-5}$ | $2.188 \cdot 10^{-3}$ | $2.146 \cdot 10^{-5}$ |
| 0625B (02) | 0.032 | $3.22 \cdot 10^{-5}$ | $7.317 \cdot 10^{-5}$ | – |
| 0703A (03) | 0.031 | $1.18 \cdot 10^{-5}$ | $1.252 \cdot 10^{-4}$ | $1.873 \cdot 10^{-5}$ |
| 0703B (03) | 0.031 | $1.30 \cdot 10^{-5}$ | $3.454 \cdot 10^{-4}$ | $2.395 \cdot 10^{-5}$ |
| 0720A (03) | 0.031 | $1.11 \cdot 10^{-5}$ | $2.008 \cdot 10^{-4}$ | $2.033 \cdot 10^{-5}$ |
| 0720B (04) | 0.030 | $1.20 \cdot 10^{-5}$ | $3.240 \cdot 10^{-4}$ | $1.834 \cdot 10^{-5}$ |
| 0728A (01) | 0.032 | $1.18 \cdot 10^{-5}$ | $1.142 \cdot 10^{-2}$ | – |
| 0728B (01) | 0.032 | $1.02 \cdot 10^{-5}$ | $2.152 \cdot 10^{-2}$ | – |
| 0731A (01) | 0.032 | $1.13 \cdot 10^{-5}$ | $1.087 \cdot 10^{-4}$ | – |
| 0731B (01) | 0.031 | $1.16 \cdot 10^{-5}$ | $2.039 \cdot 10^{-4}$ | – |

Table 4.1.: Results of the contact resistance measurements.

The silver-YBCO contact resistances listed in table 4.2 were calculated as described in section 3.5.4. The six right-hand columns contain information on the history of each sample that preceded its contact resistance measurement. For instance, the symbol "×" in the column *SP* means that the sputtering of the silver contacts was done using the standard sputtering parameters given in section 4.1.1. The two different results for sample 0424A demonstrate that glow discharge cleaning had a pronounced adverse effect on the contact resistance. The relatively high contact resistance of sample 0526A was probably caused by soldering on its silver layer, which obviously has a degrading effect on the superconductor, as discussed in section 4.3. The measurement of sample 0625A was done after attempting an anisotropy measurement, during which it was apparently damaged. A crack across one of the current contacts was discovered, which was probably responsible for the high contact

[1] In cases of low contact resistance, values measured at small currents had to be excluded due to the unreliability associated with the measurement of very small voltages.

| Sample | r ($\Omega m^2$) | $r_{Ag-YBCO}$ ($\Omega m^2$) | GD | SP | WS | G | C | BL |
|---|---|---|---|---|---|---|---|---|
| 0424A (05) | $1.551 \cdot 10^{-9}$ | $1.251 \cdot 10^{-9}$ | | | | | | |
| 0424A (18) | $5.468 \cdot 10^{-7}$ | $5.465 \cdot 10^{-7}$ | × | | | | | |
| 0526A (03) | $1.281 \cdot 10^{-8}$ | $1.251 \cdot 10^{-8}$ | | | × | | | |
| 0609A (02) | $2.756 \cdot 10^{-9}$ | $2.456 \cdot 10^{-9}$ | | | | | | |
| 0609A (04) | $4.992 \cdot 10^{-10}$ | $1.992 \cdot 10^{-10}$ | | | | × | | |
| 0625A (01) | $1.436 \cdot 10^{-8}$ | $1.406 \cdot 10^{-8}$ | | | | × | × | |
| 0625B (02) | $9.770 \cdot 10^{-10}$ | $6.770 \cdot 10^{-10}$ | | × | | × | | |
| 0703A (03) | $6.673 \cdot 10^{-10}$ | $3.673 \cdot 10^{-10}$ | | × | | × | | |
| 0703B (03) | $2.166 \cdot 10^{-9}$ | $1.866 \cdot 10^{-9}$ | | × | | × | | |
| 0720A (03) | $1.047 \cdot 10^{-9}$ | $7.473 \cdot 10^{-10}$ | | × | | × | | |
| 0720B (04) | $1.874 \cdot 10^{-9}$ | $1.574 \cdot 10^{-9}$ | | × | | | | |
| 0728A (01) | $6.730 \cdot 10^{-8}$ | $6.700 \cdot 10^{-8}$ | | × | | × | | × |
| 0728B (01) | $1.097 \cdot 10^{-7}$ | $1.094 \cdot 10^{-7}$ | | × | | × | | × |
| 0731A (01) | $5.436 \cdot 10^{-10}$ | $2.436 \cdot 10^{-10}$ | | × | | × | | |
| 0731B (01) | $1.112 \cdot 10^{-9}$ | $8.125 \cdot 10^{-10}$ | | × | | × | | |

GD = glow discharge cleaning
SP = standard parameters (sputtering)
WS = wire soldered onto silver layer
G = grooves carved into the sample
C = crack found in the sample
BL = bottom layer of the bulk cylinder

Table 4.2.: Results of the contact resistance measurements (continued).

resistance. Samples 0728A and 0728B were both cut from the bottom layer of the bulk cylinder, which is known to contain a higher density of Y-211 inclusions than the rest of the cylinder. The high contact resistances of these samples might have been caused by such inclusions, which behave like an insulator.

The six measurements from table 4.2 that were performed after similar sample preparation processes (those rows with identical "×" positions) are compared in figure 4.3. Clearly there is significant scatter among the contact resistances, resulting in a standard deviation which is greater than half of the average. The average value of the contact resistances is $1.086 \cdot 10^{-9}$ $\Omega m^2$, which is lower than the estimated requirement of $1.75 \cdot 10^{-9}$ $\Omega m^2$ mentioned in section 3.5. Typical contact resistance values of $10^{-10} \ldots 5 \cdot 10^{-10}$ $\Omega m^2$ have been reported for annealed silver conductive paint contacts on YBCO at a temperature of 77 K [2]. Since comparable contact resistances were obtained using the sample preparation method described in sections 3.1 and 3.4, the sputter deposition of silver contacts has been proven to be a viable method. Since no annealing (which causes oxygen depletion and is time-consuming) was required, sputter deposition may even be considered the superior method for contacting high-temperature superconductors.

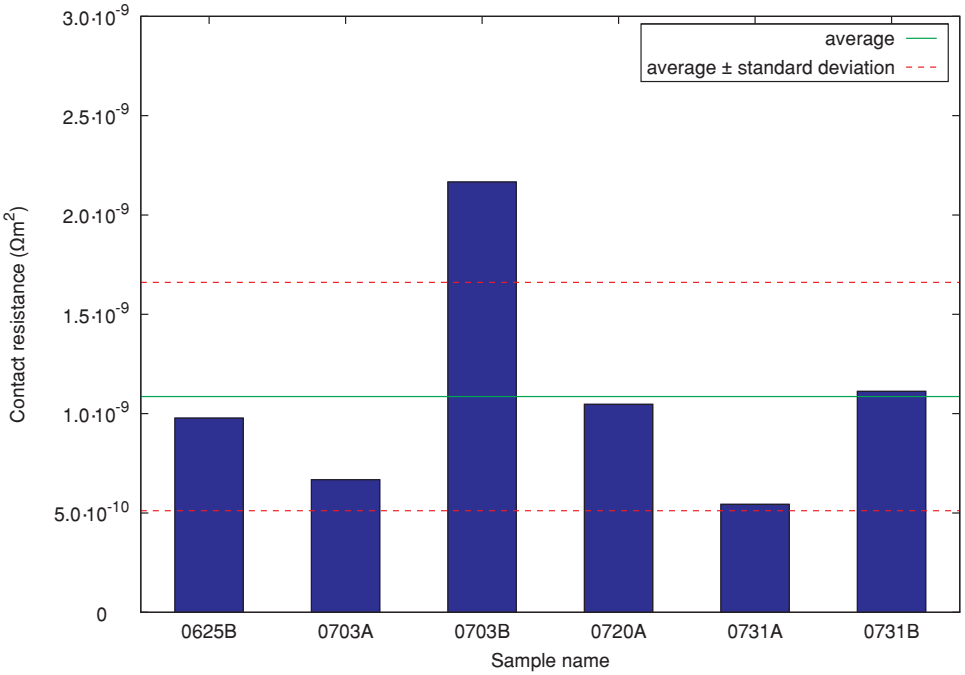


Figure 4.3.: Comparison of the contact resistances of samples that have undergone similar preparation processes.

## 4.3. Magnetoscans

A description of the magnetoscan technique and its purpose is given in section 3.6. The degrading effect of soldering, which was already mentioned in sections 3.8 and 4.2.2, becomes apparent by comparing the magnetoscans in figures 4.4 and 4.5. In the time between the two scans, a wire was soldered to one of the current contacts of sample 0526A. The degradation of the superconductor was probably caused by the formation of microscopic cracks due to the rapid temperature increase. However, chemical reactions with solder flux are also known to have a degrading effect on the material [5]. Clearly a higher magnetization was achieved before soldering. The asymmetry of the degradation (the left side of figure 4.5 is particularly dark) is consistent with the fact that due to the short soldering time the temperature increase was localized.

Figure 4.6 shows a magnetoscan of sample 0609A, which was performed directly after the YBCO bar had been glued onto its base plate. The spatial distribution of the magnetization is as expected and there are no irregularities in the scan. The crack which was found after an anisotropy measurement on this sample (see section 3.7) was obviously not present at the time of the scan.

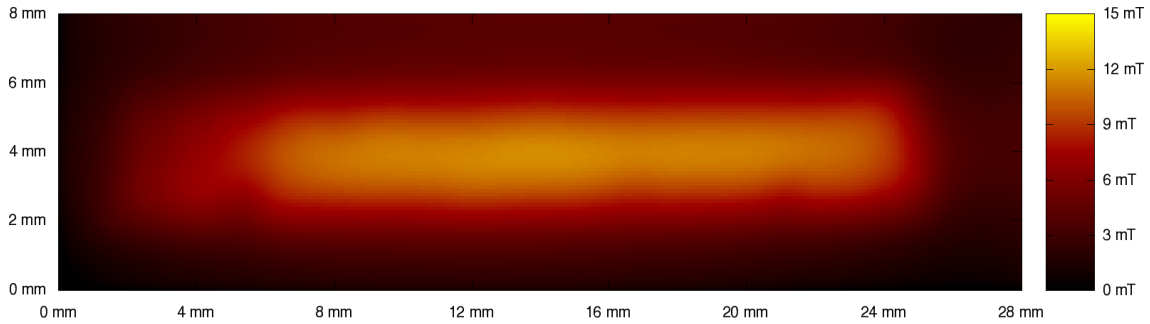


Figure 4.4.: Magnetoscan of sample 0526A before soldering.

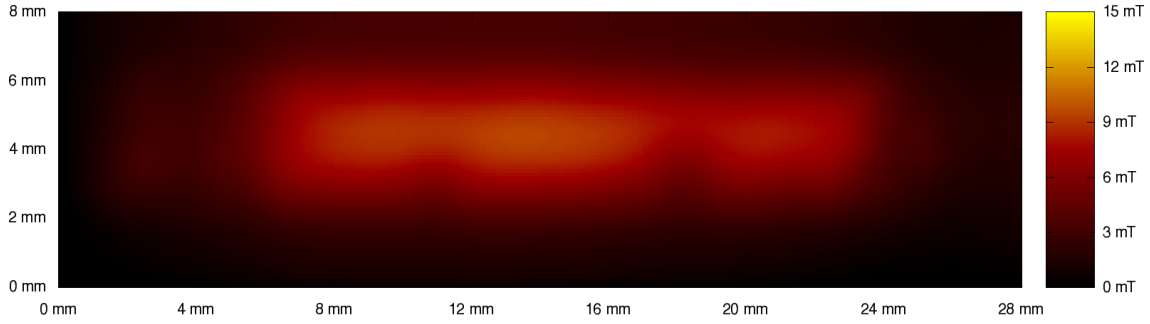


Figure 4.5.: Magnetoscan of sample 0526A after soldering a wire to its silver layer.

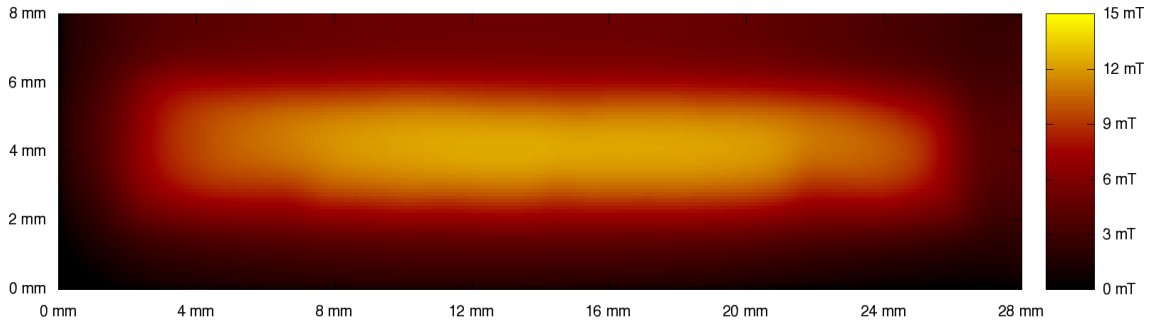


Figure 4.6.: Magnetoscan of sample 0609A performed directly after cutting and gluing the YBCO bar.

The magnetoscan depicted in figure 4.7 was performed after sputtering and milling sample 0720A. Although the bridge of the sample is clearly visible in the scan, its average magnetization is lower than expected and there are regions with particularly low magnetization on either side of the bridge as well as within the right current contact area. Since no cracks could be found, and the sample had not been exposed to temperatures or chemicals that could cause degradation, Y-211 inclusions are the most plausible explanation for the result of the magnetoscan.

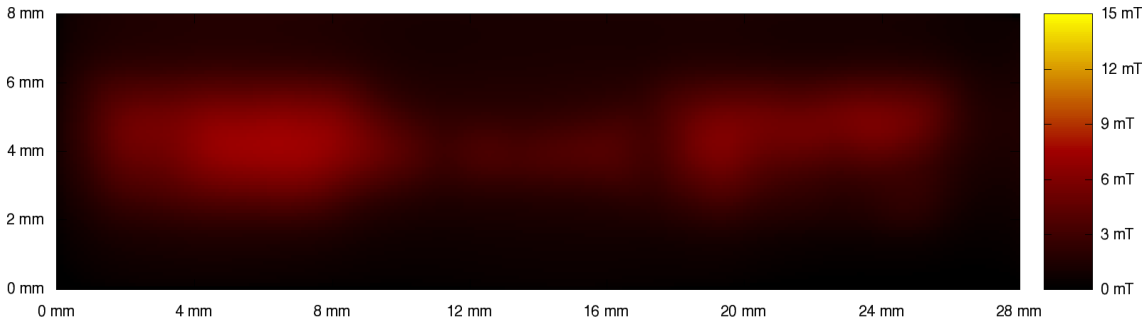


Figure 4.7.: Magnetoscan of sample 0720A, performed after sputtering and milling a bridge into the superconductor.

Figure 4.8 shows a magnetoscan of sample 0728B, which was cut from the bottom layer of the bulk cylinder. It is known that as a result of the production process (see section 2.1) the density of (RE)-211 inclusions is significantly higher at the bottom of a melt-textured bulk superconductor than at its top. The low magnitude and inhomogeneity of the magnetization in this scan are consistent with a high density of non-superconducting inclusions or bad texture (which deteriorates with increasing distance from the seed crystal).

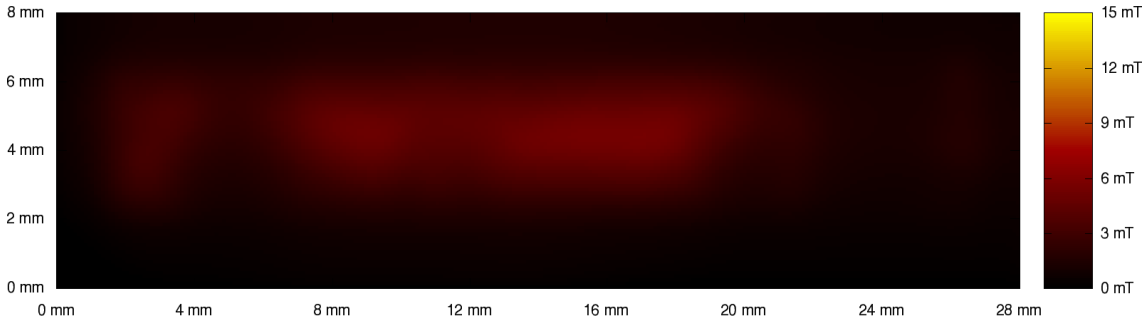


Figure 4.8.: Magnetoscan of sample 0728B. The low and inhomogeneous magnetization points to a high density of non-superconducting Y-211 inclusions or bad texture.

The magnetoscan of sample 0731A which is shown in figure 4.9 was performed after completing the anisotropy measurements on this sample. The bridge is clearly visible in the scan and the magnetization of the sample was significantly higher than that of sample 0720A (see figure 4.7). The dark region within the right current contact area may be the result of a crack that was not visible on the sample surface. Such a crack could arise from the pressure exerted by the current contacts, or it could have been in the material all along.

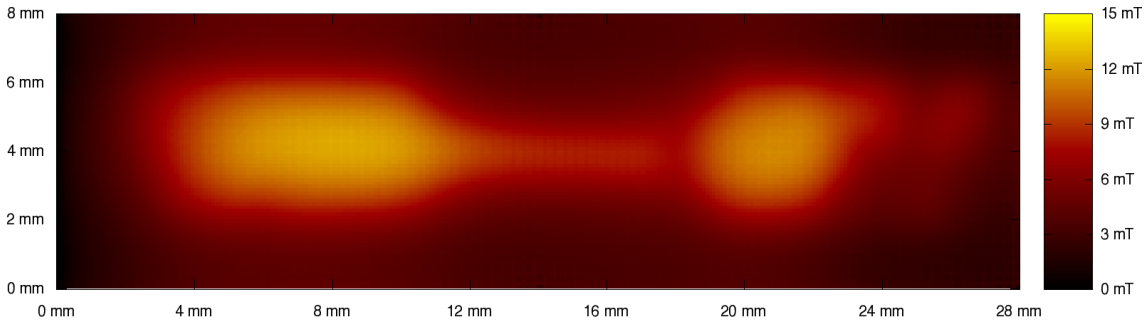


Figure 4.9.: Magnetoscan of sample 0731A.

## 4.4. Transport current anisotropy

### 4.4.1. Electromagnet system

The setup used for transport current anisotropy measurements with a water-cooled 1.4 T electromagnet is described in section 3.7.1. Such measurements were attempted with seven samples, but anisotropy curves could only be obtained in three cases. Samples 0424A and 0625A cracked while tightening the screws of the sample holder or during cooling. Sample 0703A cracked while changing the field orientation from $H \,||\, c$ to $H \,||\, ab$, which may have been caused by the $\vec{M} \times \vec{B}$ torque resulting from the magnetization of the sample. Sample 0720B was destroyed during a zero field measurement. Successful anisotropy measurements were performed with the samples 0609A, 0720A, and 0731A.

The anisotropy curves shown in this section were plotted in such a way that the orientation $H \,||\, ab$ corresponds to 0° and all plots have the same angular range of $-50 \ldots 130°$. Since the anisotropy measurements started at a different angle, a part of each anisotropy curve had to be removed from one side and attached to the other in order to produce the plots. This procedure is valid due to the 180° symmetry of the transport current anisotropy. However, in some cases a step is visible at the position

where the two parts of the curve were joined. This happens if different voltage-current curves were measured at the two end points of the 180° angle range, resulting in different $I_c$ evaluations. Possible reasons are different sample temperatures[2], and a decrease of the effective cross section of the sample during the measurement (occurrence of cracks).

Figure 4.10 shows an anisotropy curve of sample 0609A which was measured under the following conditions:

Temperature: $T = 77$ K

Magnetic field: $B = 1.4$ T

Current ramp rate: $\frac{\mathrm{d}I}{\mathrm{d}t} = 0.5$ A/s

Angular resolution: $\Phi_{step} = 1°$

Voltage criterion (for evaluation): $U_c = 0.5$ µV

The plot reveals a sharp $ab$-peak and a rounded $c$-axis peak, which is significantly smaller but clearly visible. The critical current anisotropy $\gamma_{cc}$, defined as

$$\gamma_{cc} = \frac{J_c(H \,||\, ab)}{J_c(H \,||\, c)}, \tag{4.2}$$

was 4.5 in this measurement. At the field and temperature stated above, a critical current density of approximately $2 \cdot 10^8$ A/m$^2$ can be expected for $H \,||\, c$ in a melt-textured YBCO sample [1]. Since $J_c(H \,||\, c)$ is only $5.3 \cdot 10^5$ A/m$^2$ in figure 4.10, it is plausible that the effective cross section of sample 0609A was a very small fraction (approximately 0.27%) of the measured cross section. After removing the sample from the sample rod, a crack perpendicular to the direction of the current was found, which is the most likely explanation for the small effective cross section. Since the crack was neither detected by a previous magnetoscan (see figure 4.6), nor was it visible prior to the anisotropy measurement, the sample probably cracked when tightening the screws of the sample holder or during cooling.

Sample 0720A was measured at two different magnetic fields after milling a bridge into the superconductor in order to reduce its cross section. The conditions during the first measurement were as follows:

[2] The boiling point of the liquid nitrogen at the sample position can vary due to hydrostatic pressure changes (evaporation) or oxygen pickup.

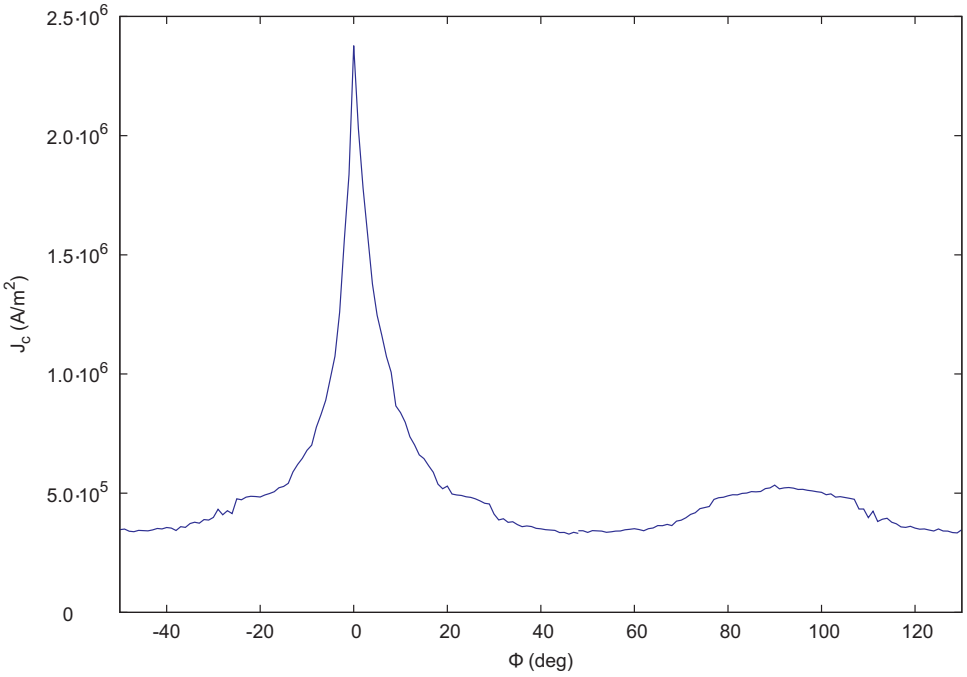


Figure 4.10.: Anisotropy curve of sample 0609A at 77 K and 1.4 T.

$T = 77$ K

$B = 1$ T

$\frac{\mathrm{d}I}{\mathrm{d}t} = 0.1$ A/s

$\Phi_{step} = 1°$

$U_c = 0.5$ µV

The conditions during the second measurement were the same except for the magnetic field and the current ramp rate:

$B = 0.5$ T

$\frac{\mathrm{d}I}{\mathrm{d}t} = 0.2$ A/s

The $c$-axis peaks of the two curves shown in figure 4.11 are almost indiscernible, which is a qualitative difference from the anisotropy curve of sample 0609A. $J_c(H \,||\, c)$ was $7.9 \cdot 10^5$ A/m$^2$ at 0.5 T and $4.1 \cdot 10^5$ A/m$^2$ at 1 T, which is again well below the expected values of approximately $3.5 \cdot 10^8$ A/m$^2$ and $2.5 \cdot 10^8$ A/m$^2$ respectively [1].

In this case the small effective cross section ($A_{eff} \approx 2 \cdot 10^{-3}\, A_{app}$) may have been caused by a large number of Y-211 inclusions (cf. magnetoscan in figure 4.7), which might also be responsible for the weak $c$-axis peaks.

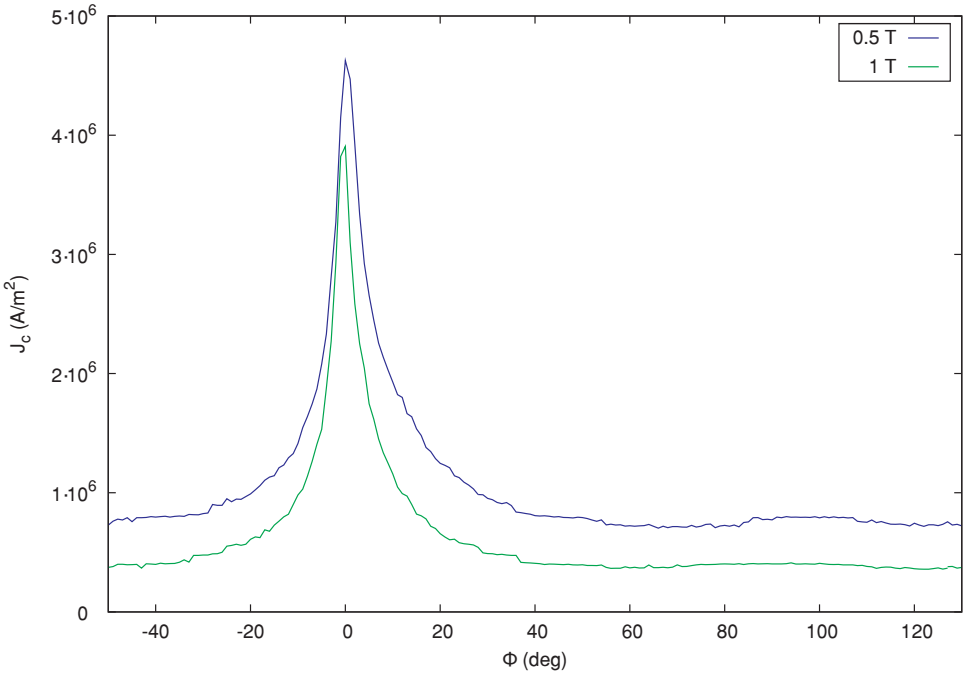


Figure 4.11.: Anisotropy curves of sample 0720A, measured at 77 K and two different magnetic fields.

The anisotropy curve shown in figure 4.12 belongs to sample 0731A and was recorded after the sample had been measured in the 6 T superconducting magnet (see section 4.4.2). The measurement was performed under the following conditions:

$T = 77$ K

$B = 1.4$ T

$\frac{\mathrm{d}I}{\mathrm{d}t} = 1$ A/s

$\Phi_{step} = 1°$

$U_c = 2$ µV

Due to the anomalous transitions (discussed in section 4.4.3) which occurred dur-

ing this anisotropy measurement, a voltage criterion of 0.5 µV would produce a very noisy plot. Therefore, $U_c = 2\,\mu V$ was used in the evaluation. Note that the $c$-axis peak of the anisotropy curve in figure 4.12 was measured before the $ab$-peak. The sample was damaged at an angle close to the $H \,||\, ab$ orientation (at $-14°$). This damage was probably caused by partial quenching of the superconductor due to heat transfer from the contact areas. The resulting Joule heating in the normal-conducting regions of the superconductor permanently damaged the material, thereby decreasing the effective cross section. A compensation for this decrease was attempted by multiplying all $J_c$ values measured after the damage had occurred by a factor of 1.075 (red curve in figure 4.12). This factor is the quotient of the $J_c$ values measured directly before and after the step in the graph.

There are two qualitative differences between the anisotropy curve of sample 0731A and those of the samples 0609A and 0720A. The first one is the rounded $ab$-peak in the plot belonging to sample 0731A. The most plausible explanation for this behavior are thermally induced transitions. In other words, the Joule heating in the contact areas, which was significantly higher for this sample due to the higher transport current density, caused a temperature increase of the superconductor, which lowered the critical current. The occurrence of anomalous transitions in this measurement and the temperature increase which was found during the measurements in the superconducting magnet (see section 4.4.2) support this explanation. The comparatively high transport current density of sample 0731A may have been the result of its low amount of inclusions (it was cut from the top of the bulk cylinder). This correlation was also reported in [2]. The second difference between the anisotropy curve in figure 4.12 and the previously measured ones is the low $\gamma_{cc}$ value of 1.15 (calculated with the corrected data). This is obviously a consequence of the rounded $ab$-peak. If the peak had not been "ablated" by thermally induced transitions, $\gamma_{cc}$ would be significantly higher.

A second measurement of the transport current anisotropy of sample 0731A was performed under the same conditions except for the current ramp rate, which was increased to 5 A/s. This was done in order to reduce the Joule heating by shortening the time required for measuring the individual voltage-current curves. As shown in figure 4.13, the results for the $c$-axis peak (which was again measured before the $ab$-peak) were within 10% of the $J_c$ values found in the first measurement. The graph is noisier than the one in figure 4.12 because a higher current ramp rate goes along with less points in each voltage-current curve, thereby decreasing the accuracy of the $I_c$ evaluation. Unfortunately, the sample was severely damaged while measuring the $ab$-peak (at $-17°$ in the graph). The damage was probably caused by partial quenching, just like in case of the previous anisotropy measurement of sample 0731A. Even so, the shape of the slopes left and right from the step in the graph suggests that a sharp peak with a maximum $J_c$ value well above that of the $c$-axis peak would have been measured if the damage had not occurred. This result supports the claim that the rounded $ab$-peak in figure 4.12 was caused by thermally induced transitions.

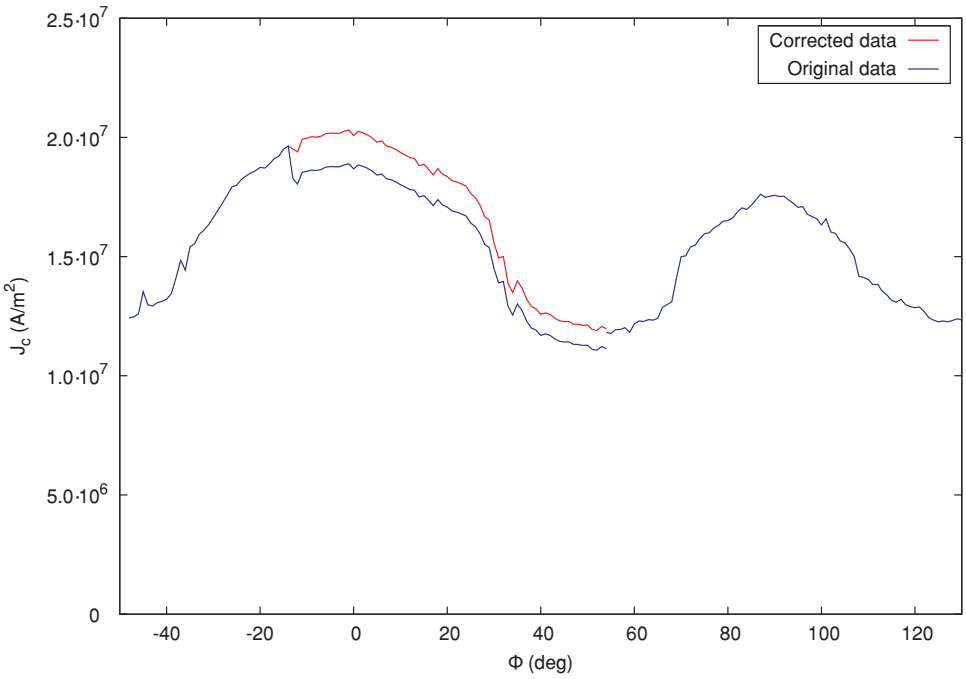


Figure 4.12.: Anisotropy curve of sample 0731A, measured at 77 K and 1.4 T. The corrected data was calculated by taking the reduction of the effective cross section into account.

Multiplying the value of $J_c$ at 0° in figure 4.13 with the quotient of the values directly before and after the step, yields an approximate value of $8.3 \cdot 10^7$ A/m$^2$ for the hypothetical *ab*-peak of the undamaged sample.

### 4.4.2. Superconducting 6 T magnet system

Anisotropy measurements in a 6 T superconducting magnet system equipped with a helium gas flow cryostat (see section 3.7.2) were attempted with the samples 0720A and 0731A. The former exhibited extremely small critical currents which rendered the measurements useless. When the sample was removed from the cryostat, it was discovered that its bridge was almost completely destroyed (see figure 3.33). The damage was probably the result of mechanical stress caused by the temperature gradient that was present during cooling. Sample 0731A was cooled at a painfully slow rate of 0.5 K/min in order to minimize the risk of losing another sample. The transport current anisotropy of this sample was successfully measured at a temperature of 77 K and different magnetic fields. The series of measurements whose results are depicted in figure 4.14 was performed under the following conditions:

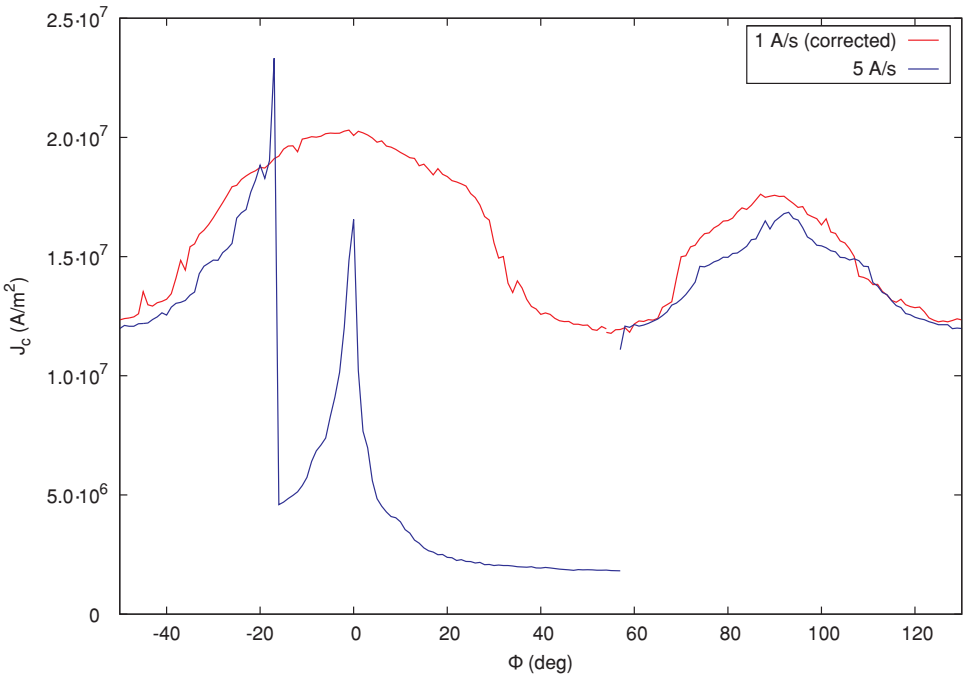


Figure 4.13.: Two anisotropy curves of sample 0731A, measured with different current ramp rates. Temperature and magnetic field were 77 K and 1.4 T in both cases.

$T = 77$ K

$B = 2$ T, 3 T, 4 T, 5 T, 6 T

$\Phi_{step} = 1°$

$U_c = 1$ µV

A voltage criterion of 1 µV was chosen because 0.5 µV would have resulted in too much noise due to anomalous transitions (see section 4.4.3). The current ramp rate is not given, since the control software of the superconducting magnet automatically adjusts its value based on an initial value and the desired number of points within each voltage-current curve.

The anisotropy curves measured at 2 T and 3 T seem to have no *c*-axis peak, which is an unfortunate consequence of choosing $U_c = 1$ µV. The *c*-axis peaks of these curves are noticeable if the evaluation is done with a lower voltage criterion, such as $U_c = 0.5$ µV. However, the curves would be extremely noisy in this case. The anisotropy curves measured at 2 T, 3 T, and 4 T have rounded *ab*-peaks, similar

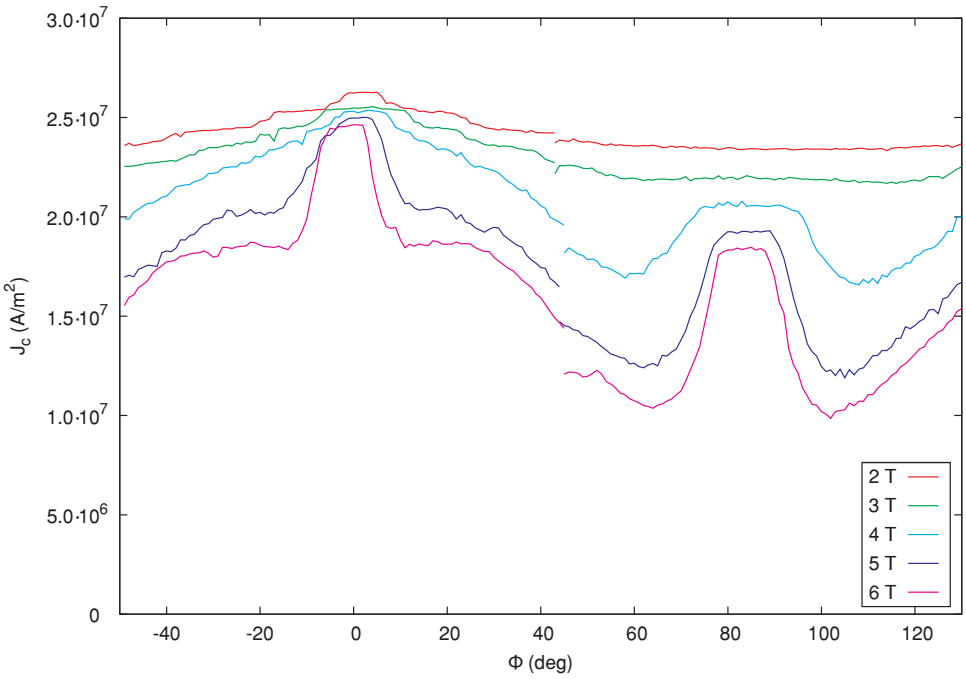


Figure 4.14.: Anisotropy curves of sample 0731A, measured at 77 K and five different magnetic fields.

to the result of the measurement on sample 0731A in the electromagnet at 1.4 T (see figure 4.12). The 5 T and 6 T curves have distinctive "bumps" at the center of their *ab*-peaks, which are a result of the field dependence of the peak shape. The *ab*-peaks are more pronounced at higher magnetic fields [2]. However, due to thermally induced transitions the maximum current density is almost identical for all anisotropy curves, which results in peculiarly shaped *ab*-peaks at higher fields.

Judging from the five plots in figure 4.14, the position of the *ab*-peak appears to shift towards negative angles with increasing field. This cannot be the effect of a positioning error, since the Hall probe of the sample rod was used to determine the $H \,||\, ab$ orientation for each plot. The center of the *ab*-peak of the 2 T curve appears to be located at $+2°$, whereas the *ab*-peak of the 6 T curve is at $-2°$. Thus, assuming a linear dependence, the resulting peak shift is

$$s = \frac{\Delta\Phi}{\Delta B} = \frac{-2° - 2°}{6\ \mathrm{T} - 2\ \mathrm{T}} = -1°/\mathrm{T}. \tag{4.3}$$

Another interesting fact is that the *c*-axis peaks appear to be centered at 84°. Due to the very small 2 T and 3 T *c*-axis peaks, it is not possible to determine whether the *c*-axis peaks also experienced a field dependent shift or not. Nevertheless, the difference in position of the *ab*-peaks and the *c*-axis peaks is less than 90° in the three plots for which it can be determined. The reason for this phenomenon is currently

unknown. It may have to do with misalignments of the grains within the sample, but this is speculation.

The helium gas flow cryostat used for these measurements was filled with liquid nitrogen in order to determine whether the results would differ from gas flow cooling. Anisotropy measurements at two previously used field settings were repeated with liquid nitrogen cooling. The conditions for the first measurement were as follows:

$T = 77$ K ($LN_2$ cooling)

$B = 3$ T

$\Phi_{step} = 1°$

$U_c = 1$ µV

The second measurement was performed under these conditions:

$T = 77$ K ($LN_2$ cooling)

$B = 4$ T

$\Phi_{step} = 3°$

$U_c = 1$ µV

The results of these two measurements as well as the corresponding previously measured anisotropy curves are depicted in figure 4.15. While the shapes of the curves do not differ significantly, the $J_c$ values within the peaks were higher (up to 12%) in case of liquid nitrogen cooling at both fields. This result suggests that the higher thermal conductivity of liquid nitrogen slowed down the heating of the sample, allowing it to reach a higher transport current before thermally induced transitions occurred. This conclusion is supported by the fact that the maximum temperature increase within each voltage-current curve (measured with the sensor near the sample) was approximately 30 mK, as opposed to 200 mK in case of gas flow cooling.

One anisotropy measurement on sample 0731A was performed at a higher temperature setting in order to demonstrate the profound impact of the sample temperature. The conditions for this measurement were as follows:

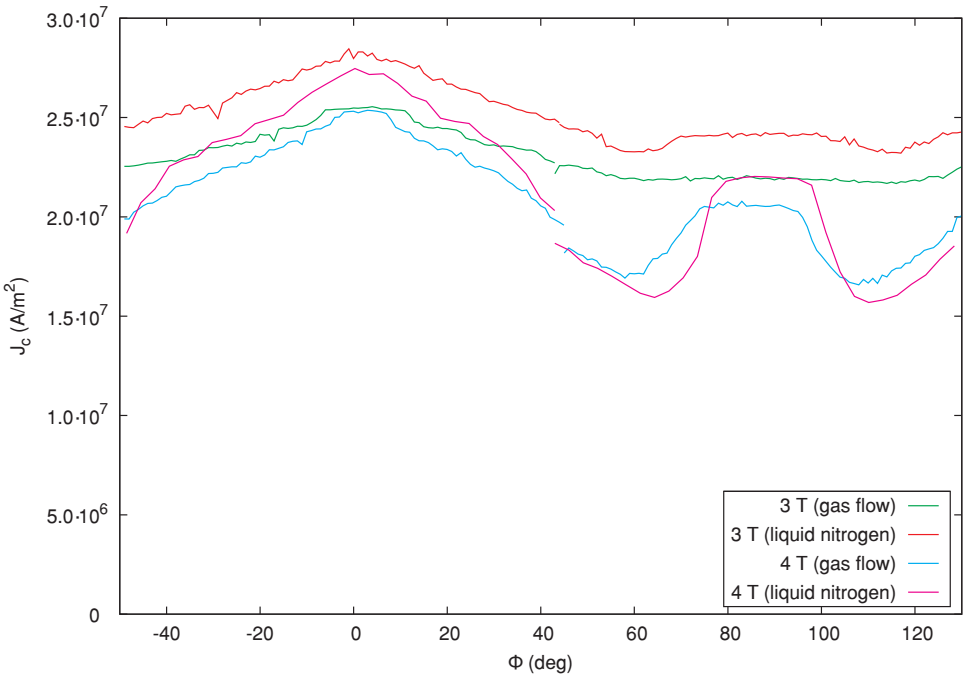


Figure 4.15.: Comparison of anisotropy curves measured with helium gas flow cooling and liquid nitrogen cooling.

$T = 82$ K

$B = 6$ T

$\Phi_{step} = 1°$

$U_c = 1$ µV

Figure 4.16 shows the result of the 82 K measurement. The anisotropy curve does not extend over the full 180° range, since the critical current density outside the displayed region was too small to be measured. Just like the 5 T and 6 T curves measured at 77 K (see figure 4.14), this anisotropy curve has a bump at the center of its *ab*-peak. In this case the bump is more pronounced and a sharp local minimum is superimposed on it, which may be the result of anomalous transitions.

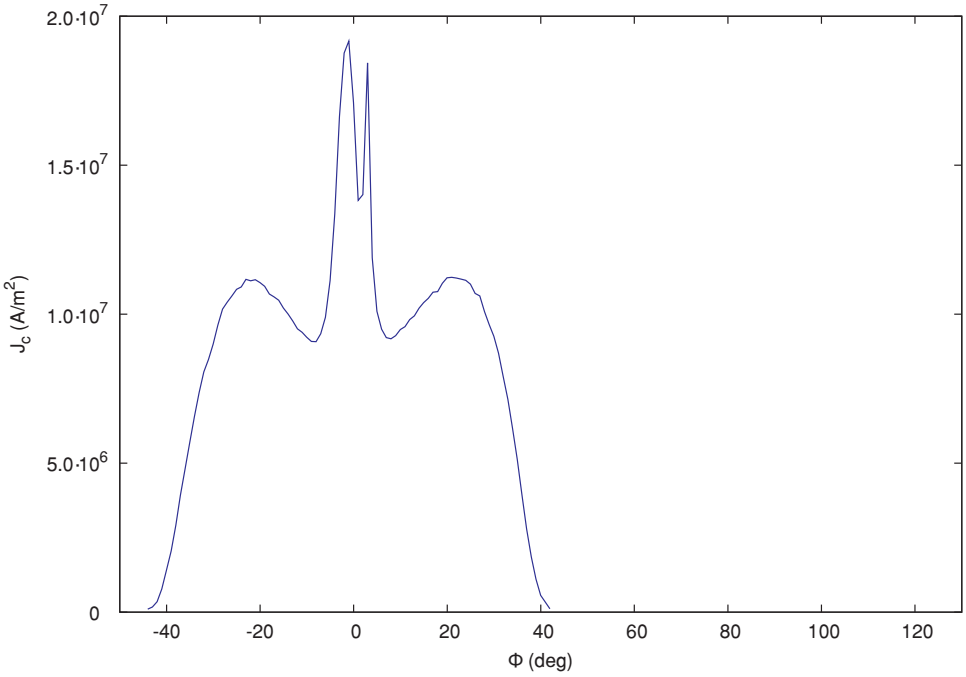


Figure 4.16.: Anisotropy curve of sample 0731A, measured at 82 K and 6 T.

### 4.4.3. Anomalous transitions

The transitions from the superconducting to the dissipative state that occur in high-temperature superconductors, have a distinctive voltage-current characteristic. It can usually be approximated by a power law:

$$U(I) = k\, I^n \tag{4.4}$$

$U(I)$ is the voltage measured between two points (voltage contacts) along the path of the current $I$, whereas $k$ and $n$ are fit parameters. Such power law fit functions are calculated for each voltage-current curve within a given anisotropy measurement by the Scilab evaluation function previously mentioned. During the anisotropy measurements presented in sections 4.4.1 and 4.4.2, transitions which significantly deviate from the calculated fit functions were found.

The voltage-current curve in figure 4.17 was taken from the anisotropy measurement on sample 0609A in the electromagnet (see figure 4.10). It was measured at the $H \,||\, ab$ orientation ($\Phi = 0°$ in the anisotropy plot), and the fit parameters are $k = 4.162 \cdot 10^{-5}$ and $n = 6.073$. Obviously the power function is a good approximation of this voltage-current curve, which can therefore be considered as a regular transition.

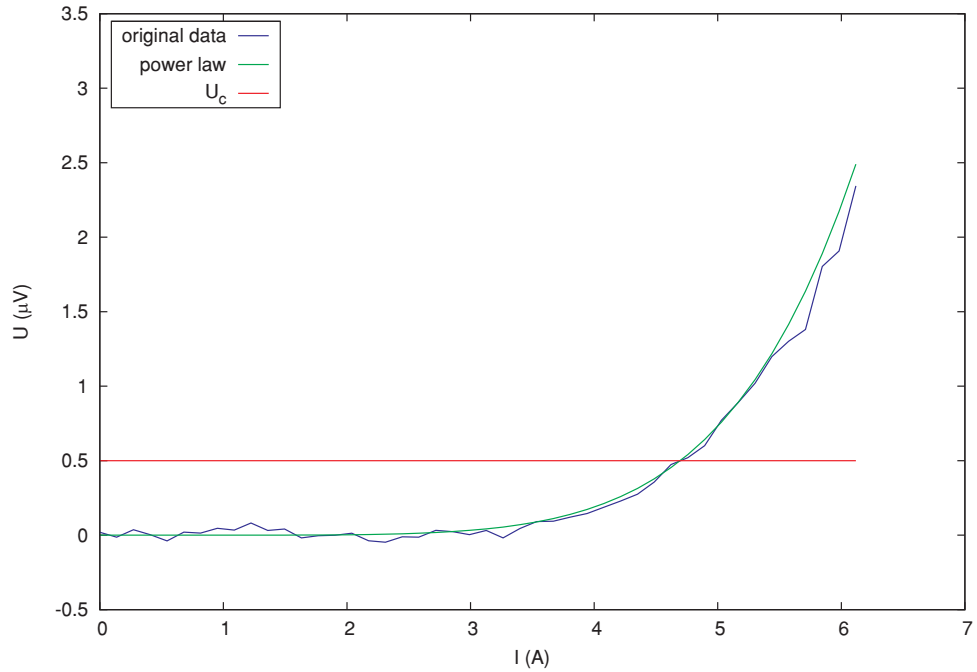


Figure 4.17.: Voltage-current curve of sample 0609A, measured at 77 K, 1.4 T, 0° (center of the *ab*-peak).

Figure 4.18 shows a voltage-current curve of sample 0731A, which was measured with the electromagnet system. Again, the orientation was $H \,||\, ab$ while this particular curve was measured, and the fit parameters are $k = 9.920 \cdot 10^{-25}$ and $n = 16.936$. Clearly the power fit function is not a very suitable approximation in this case, which is why this transition can be regarded as anomalous.

The two voltage-current curves in figure 4.19 were taken from the 4 T anisotropy measurement of sample 0731A, which was performed in the superconducting magnet (see figure 4.14). The curve which was recorded between the *ab*-peak and the *c*-axis peak ($\Phi = 56°$ in the anisotropy plot) exhibits only a moderate deviation from its power law fit function ($k = 5.007 \cdot 10^{-13}$, $n = 8.912$). The other curve, which was recorded at the center of the *c*-axis peak ($\Phi = 84°$), deviates significantly from its fit function ($k = 4.897 \cdot 10^{-30}$, $n = 20.090$) and can therefore be considered as anomalous.

Figure 4.20 shows two voltage-current curves of sample 0731A, which were measured in the superconducting magnet at a temperature of 82 K. The corresponding anisotropy curve is shown in figure 4.16. One of the curves was taken from the position where the *ab*-peak in the anisotropy curve has a notch ($\Phi = 1°$). Although the power law fit function ($k = 2.851 \cdot 10^{-8}$, $n = 5.867$) approximates this curve quite well near the critical current, there is a distinctive deviation at low currents.

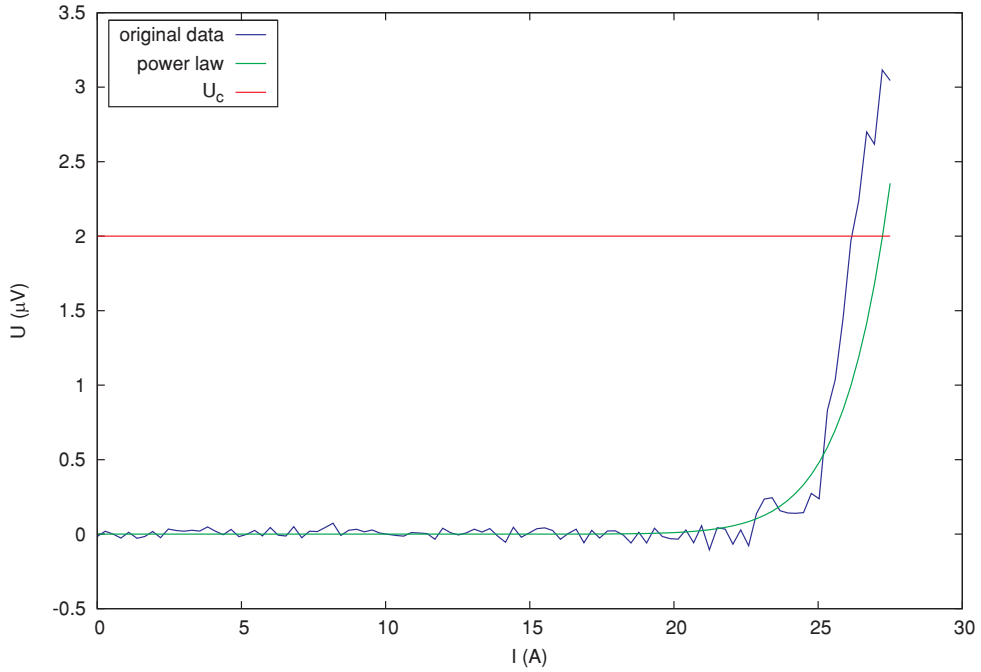


Figure 4.18.: Voltage-current curve of sample 0731A, measured at 77 K, 1.4 T, 0° (center of the *ab*-peak).

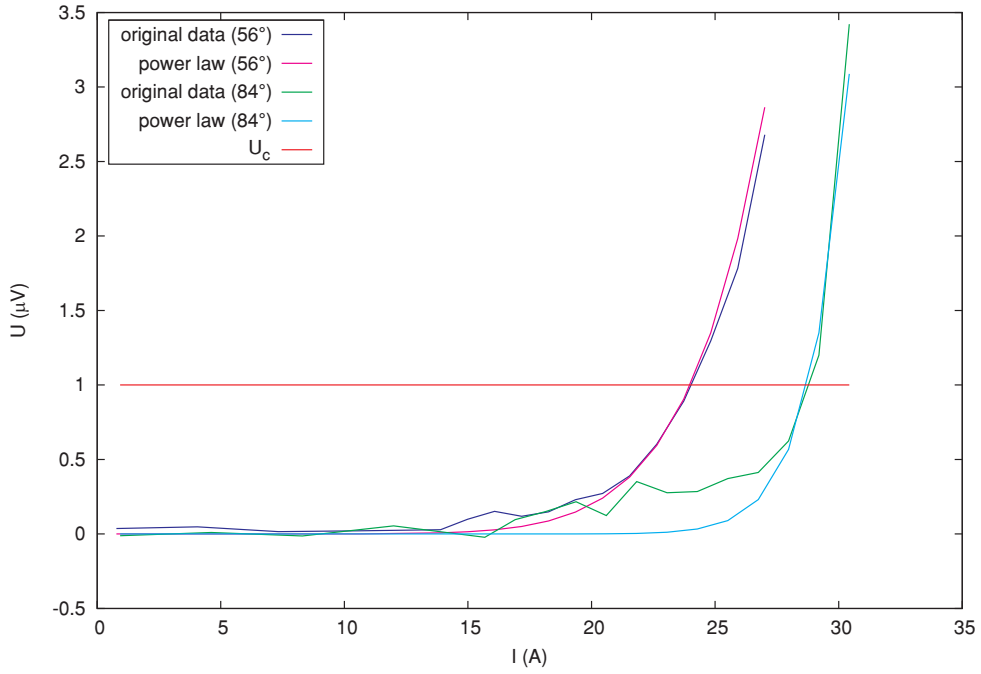


Figure 4.19.: Voltage-current curves of sample 0731A, measured at 77 K, 4 T, 56° (between the peaks) / 84° (center of the *c*-axis peak).

This behavior may suggest that the transition was anomalous, which would explain the otherwise mysterious notch in the anisotropy curve. The other voltage-current curve, which was taken from the left slope of the *ab*-peak in figure 4.16, does not deviate much from its fit function ($k = 2.280 \cdot 10^{-3}$, $n = 3.546$) and can therefore be considered as regular.

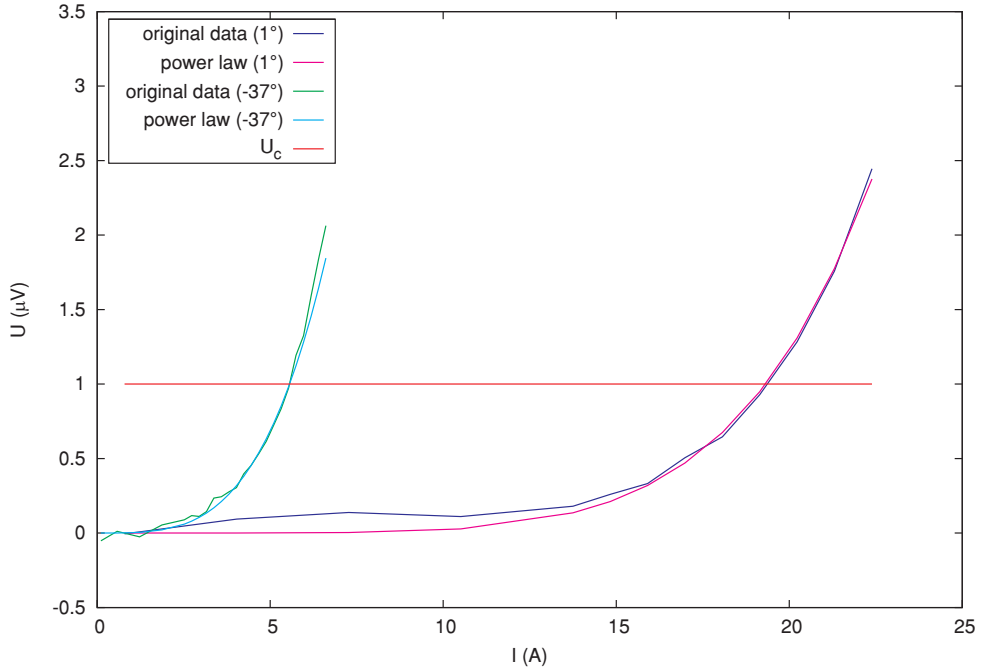


Figure 4.20.: Voltage-current curves of sample 0731A, measured at 82 K, 6 T, 1° (center of the *ab*-peak) / −37° (slope of the *ab*-peak).

Summarizing these results, it can be stated that some of the transitions within the measured anisotropy curves exhibited the expected characteristics (regular transitions), whereas others did not (anomalous transitions). The latter can be identified by their deviation from the power law (4.4) and their relatively high $n$ values (typically 10 ... 50, whereas the $n$ values of regular transitions usually were below 10). High critical current densities facilitate the occurrence of anomalous transitions. This is consistent with the previously mentioned theory that these transitions are thermally induced, i. e. they occur because of an increase of the sample temperature due to Joule heating in the contact areas. Since the expected $J_c$ values are particularly high for the orientations $H \,||\, ab$ and $H \,||\, c$, the effect of thermally induced transitions on the shape of the anisotropy curves is most pronounced for these orientations. This circumstance leads to the observed ablation of the peaks in the anisotropy curves depicted in the figures 4.12, 4.13, 4.14, 4.15, and 4.16.

# 5. Conclusions

A brief summary of the most important results contained in the diploma thesis at hand is given in the following:

- A sample preparation method for YBCO bulk superconductors, which yields reproducible results in terms of contact resistance, was developed.
- A sample tray for the sputtering machine of the institute, which is suitable for different sample geometries, was constructed.
- A silver-YBCO contact resistance comparable to the values reported in [2] was achieved by means of sputter deposition.
- It was demonstrated that soldering on the silver layer of a sample degrades the superconductor underneath.
- The transport current anisotropy of melt-textured YBCO bulk samples was successfully measured at different magnetic fields.
- The difference between liquid nitrogen cooling and helium gas flow cooling as well as the influence of the current ramp rate was investigated.
- The observed ablation of the peaks in some of the anisotropy curves could be ascribed to the occurrence of thermally induced transitions, which is in agreement with the experimental data.

On a personal level, I find it noteworthy that this diploma thesis helped me expand my horizons in terms of scientific research and writing. Furthermore, it gave me the opportunity to learn how to operate the equipment required for the sample preparation and measurements described above. I would like to close with some thoughts on possible improvements of the discussed experimental methods:

- Even lower contact resistance values might be attained by refining the surface treatment. A machine that carves very fine grooves into the surface of the bulk superconductor could be such a refinement.

- A sample rod with massive copper electrode blocks might help to avoid thermally induced transitions during anisotropy measurements because of its greater heat capacity. By embedding a temperature sensor into one of these electrode blocks, the temperature increase due to Joule heating in the contact areas could be measured more accurately.

- Research on the detrimental influence of glow discharge cleaning on the silver-YBCO contact resistance could provide valuable insights.

# 6. Bibliography


[1] D.A. Cardwell, N. Hari Babu, *Processing and properties of single grain (RE)–Ba–Cu–O bulk superconductors*, Physica C **445—448** (2006) 1–7

[2] D. Braithwaite, D. Bourgault, N. Schopohl, R. Tournier, J.M. Barbut, J.C. Vallier, *The Angular Dependence of Critical Current Densities in Bulk Magnetically Melt Textured YBaCuO in Magnetic Fields up to 20 Teslas*, Journal of Low Temp. Phys. **92**, 5/6, (1993) 295–305

[3] Michael Eisterer, *Hochtemperatursupraleiter* lecture slides

[4] R.L. Barns, R.A. Laudise, *Stability of superconducting $YBa_2Cu_3O_7$ in the presence of water*, Appl. Phys. Lett. **51** (1987) 1373–1375

[5] Jack W. Ekin, *Experimental Techniques for Low-Temperature Measurements*, Oxford University Press (2006), ISBN: 978-0-19-857054-7

[6] M. Zeisberger, I. Latka, W. Ecke, T. Habisreuther, D. Litzkendorf, W. Gawalek, *Measurement of the thermal expansion of melt-textured YBCO using optical fibre grating sensors*, Supercond. Sci. Technol. **18** (2005) S202–S205

[7] Milton Ohring, *Materials Science of Thin Films*, Academic Press (2002), ISBN: 978-0-12-524975-1

[8] Roland Zengerle, *Dünnschichttechnik* lecture slides

[9] D. Depla, S. Mahieu, R. De Gryse, *Magnetron sputter deposition: Linking discharge voltage with target properties*, Thin Solid Films **517** (2009) 2825—2839

[10] M. Eisterer, S. Haindl, T. Wojcik, H.W. Weber, *'Magnetoscan': a modified Hall probe scanning technique for the detection of inhomogeneities in bulk high temperature superconductors*, Supercond. Sci. Technol. **16** (2003) 1282–1285.